THE GEOLOGICAL SOCIETY OF AMERICA®

A 9 million-year-long astrochronological record of the early–middle Eocene corroborated by seafloor spreading rates

Federica Francescone[1,†], Vittoria Lauretano[2,§], Claire Bouligand[3,§], Matteo Moretti[1,§], Nadia Sabatino[4,§], Cindy Schrader[5,§], Rita Catanzariti[6,§], Frits Hilgen[5,§], Luca Lanci[1,§], Antonio Turtù[7,§], Mario Sprovieri[4,§], Lucas Lourens[5,§], and Simone Galeotti[1,§]

[1]*Dipartimento di Scienze Pure e Applicate, Università di Urbino, Campus Scientifico "E. Mattei," 61029 Urbino, Italy*
[2]*School of Chemistry, University of Bristol, Cantock's Close, Bristol, BS8 1TS, United Kingdom*
[3]*Université Grenoble Alpes, Université Savoie Mont Blanc, Centre National de Recherche Scientifique (CNRS), Institut de Recherche pour le Développement (IRD), Institut Français des Sciences et Technologies des Transports (IFSTTAR), et Institut des Sciences de la Terre (ISTerre), 38000 Grenoble, France*
[4]*Istituto per l'Ambiente Marino Costiero, Consiglio Nazionale delle Ricerche (IAMC-CNR), Capo Granitola, Via del Mare 3, 91021 Campobello di Mazara (Tp), Italy*
[5]*Department of Earth Sciences, Faculty of Geosciences, Utrecht University, Heidelberglaan 2, 3584 CS, Utrecht, The Netherlands*
[6]*Istituto di Geoscienze e Georisorse, Consiglio Nazionale delle Ricerche (CNR), Via G. Moruzzi 1, 56124, Pisa, Italy*
[7]*Department of Earth and Life Sciences, Vrije Universiteit, De Boelelaan 1085, 1081 HV Amsterdam, The Netherlands*

ABSTRACT

The early–middle Eocene (ca. 56–41 Ma) is recorded in the pelagic Scaglia Rossa and Variegata Formations of the Umbria-Marche Basin (central Italy). Geochemical and magnetostratigraphic alignment between the Bottaccione section (Gubbio, central Italy) and the Smirra core (Cagli, central Italy) allows us to generate a continuous and well-preserved new record that, combined with previously published data from the same area, creates a continuous high-resolution record from the Paleocene-Eocene thermal maximum (ca. 56 Ma) to the lower part of chron C21n. Comparison with carbon isotope records from Ocean Drilling Program Sites 1258 and 1263 reveals a satisfactory match, providing further evidence of the global significance of the long-term trend and superposed perturbations captured by the $\delta^{13}C$ records. The identification of astronomically forced geochemical cycles allows us to develop a 405 k.y. tuned age model, thereby extending the astrochronology from ca. 56.0 to ca. 47.5 Ma. Marine magnetic anomaly profiles from major oceanic basins characterized by high seafloor spreading rates were used to independently test the astronomical polarity time scale associated with our tuning, as well as other polarity time scales. Our age model suggests the existence of periods of relatively constant seafloor spreading rates separated by rapid changes, while the other time scales generate more gradual variations and also include large and short-term deviations in spreading rates that occur simultaneously in different oceanic basins, implying errors in polarity reversal ages. The Umbria-Marche age model further contributes to the closure of the middle Eocene gap in the astronomical time scale.

INTRODUCTION

The early–middle Eocene (ca. 56–41 million years ago or Ma) time interval was characterized by a series of transient global warming events, recorded in both marine and continental settings. These short-lived (10^4–10^5 yr) events, known as hyperthermals, were linked to large perturbations in the global carbon cycle, marked by carbon isotope excursions (CIEs), which track the injection of massive amounts of isotopically light carbon into the exogenic carbon pool (Lourens et al., 2005; Zachos et al., 2005, 2010; Nicolo et al., 2007; Westerhold and Röhl, 2009; Galeotti et al., 2010, 2017). The most important of these events was the Paleocene-Eocene thermal maximum, or Eocene thermal maximum 1 (ETM1) at ca. 56 Ma, ETM2 at ca. 54 Ma, and ETM3 at ca. 52.8 Ma (Kennett and Stott, 1991; Röhl et al., 2004; Lourens et al., 2005; Tripati and Elderfield, 2005; Zachos et al., 2005; Westerhold et al., 2007; Sluijs et al., 2008; Galeotti et al., 2010, 2017; Dunkley-Jones et al., 2013). CIEs are associated with increased temperature, recorded as negative excursions in oxygen isotope records, and concomitant $CaCO_3$ dissolution/dilution observed in deep-sea and shallow-marine successions. The records show a remarkable imprint of astronomically forced geochemical and lithological cycles (Galeotti et al., 2010, 2015, 2017; Sexton et al., 2011; Kirtland Turner et al., 2014; Lauretano et al., 2015, 2016; Westerhold et al., 2017). These cycles have provided a robust astrochronological framework for the early Paleogene through their calibration to eccentricity target curves calculated by means of the newest La2010 and La2011 solutions (Laskar et al., 2011a, 2011b; Westerhold et al., 2012, 2017). A robust astrochronological time frame is critical for fully understanding the dynamics related to hyperthermal events and to aid in closing the Eocene gap in the astronomical time scale, or ATS (Pälike and Hilgen, 2008). However, uncertainties still affect the time scale, partly due to the scarcity of well-exposed and continuous

†Corresponding author: federica.francescone@uniurb.it.
§E-mails: vittoria.lauretano@bristol.ac.uk; claire.bouligand@univ-grenoble-alpes.fr; matteo.moretti@uniurb.it; nadia.sabatino@gmail.com; C.D.Schrader@uu.nl; r.catanzariti@igg.cnr.it; F.J.Hilgen@uu.nl; luca.lanci@uniurb.it; a.turtu@vu.nl; mario.sprovieri@iamc.cnr.it; L.J.Lourens@uu.nl; simone.galeotti@uniurb.it.

GSA Bulletin; March/April 2019; v. 131; no. 3/4; p. 499–520; https://doi.org/10.1130/B32050.1; 14 figures; 6 tables; published online 1 November 2018.

geochemical and magnetostratigraphic records, in particular across the silica-rich (McGowran, 1989) early Eocene climatic optimum interval (see also Lauretano et al., 2016; Galeotti et al., 2017). The bathyal pelagic Scaglia Rossa Formation in the Umbria-Marche Basin has produced an exceptionally well-preserved and continuous magnetobiostratigraphic record of the entire Paleogene. Astronomically controlled cycles provide a robust cyclochronology for the early Paleocene, corresponding to magnetochrons C29r to C27n (Galeotti et al., 2015), and the early Eocene, corresponding to magnetochrons C24r-C23n (Galeotti et al., 2010, 2017). Here, we extend the already available cyclochronological record of the continuous Scaglia Rossa Formation by analyzing the interval spanning magnetochron C22r to C21n (ca. 50.5–47.5 Ma) in the Bottaccione section (Gubbio, Italy) and in the newly drilled Smirra core (Turtù et al., 2017). Our results, together with previous data from the Contessa Road–Bottaccione composite section (Galeotti et al., 2010, 2017), provide a continuous 9-m.y.-long astrochronological record of the Scaglia Rossa Formation spanning from the Paleocene-Eocene thermal maximum to the lower part of C21n. Finally, we compare the temporal variations of seafloor spreading in different oceanic basins estimated from the resulting polarity time scale and from other time scales. For this purpose, we used a database of chron widths derived from sea-surface magnetic anomaly profiles (Bouligand et al., 2006) and recently published seafloor spreading curves (Cande and Patriat, 2015; Wright et al., 2016b). The minimization of seafloor spreading variations at multiple localities has long been used as a tool for constructing, refining, or correcting the polarity time scale (e.g., Cande and Kent, 1992; Huestis and Acton, 1997; Malinverno et al. 2012; Cande and Patriat, 2015). Here, we prefer to use seafloor spreading rates as a test of the polarity time scale, with the idea that large and short-term deviations in seafloor spreading rate that occur simultaneously in all the basins point to an error in the time scale. This approach has previously been successfully applied in constructing the Neogene ATS (e.g., Wilson, 1993; Krijgsman et al., 1999).

GEOLOGICAL SETTING

Bottaccione Section

In the Umbria-Marche Basin (Italy), the Lower to Middle Eocene is locally preserved in the pelagic Scaglia Rossa Formation, characterized by the alternation of well-bedded pink to reddish pelagic limestones and marly limestones. In this study, we extend previously published results from the original sample set of Galeotti et al. (2017), focusing on the well-known Tethyan succession of the Bottaccione (BTT) section at Gubbio (lat. 43°21′56″N, long. 12°34′57″E; central Italy; Fig. 1B; Arthur and Fischer, 1977; Napoleone et al., 1983; Galeotti et al., 2015, 2017). The studied 15 m interval, spanning 63.6–78.4 m above the Cretaceous-Paleogene boundary (level 0 of the log in Galeotti et al., 2000), therefore extends the available Lower Eocene stratigraphy of Galeotti et al. (2010, 2017) to the top of magnetochron C21r, obtaining an ~48-m-thick continuous and well-preserved record that spans the interval from the Paleocene-Eocene thermal maximum to the upper part of magnetochron C21r.

Smirra Core

The Lower to Middle Eocene stratigraphic interval is also well exposed in a small abandoned quarry close to the village of Smirra (lat. 43°35′09.40″N, long. 12°40′37.30″E), in the Umbria-Marche Basin (Fig. 1B). The Lower

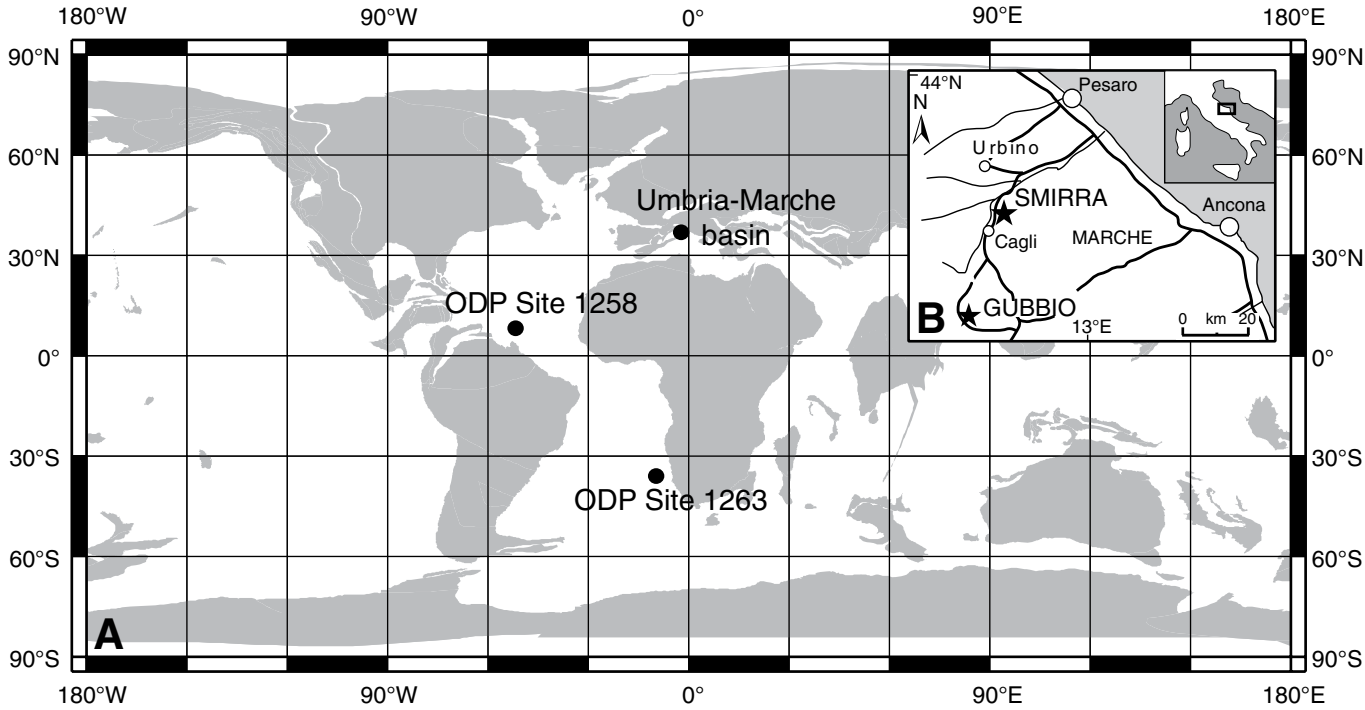

Figure 1. (A) Paleoceanographic reconstruction for the early Eocene (50 Ma) showing the position of the Umbria-Marche Basin, Ocean Drilling Program (ODP) Site 1258, and ODP Site 1263. Paleogeographic map is from the Ocean Drilling Stratigraphic Network Plate Tectonic Reconstruction Service (http://www.odsn.de/odsn/services/paleomap/paleomap.html). (B) Location map of Gubbio (lat. 43°21′56″N; long. 12°34′57″E) and Smirra (lat. 43°35′09.40″N; long. 12°40′37.30″E).

Eocene succession is represented by the Scaglia Rossa Formation, while the Middle Eocene is recorded by the overlying Scaglia Variegata Formation, composed of whitish to reddish marly limestones and marls with a significant increase in the siliciclastic fraction (~20%–30%). In this work, we focus on the succession recovered in hole 1, hereinafter referred to as Smirra 1, or S1, consisting of 41 m of rock drilled from the top of the exposed outcrop of the quarry, corresponding to level 0 in the log (for more details, see Turtù et al., 2017).

MATERIALS AND METHODS

Magnetostratigraphy

A high-resolution magnetostratigraphic record of the Contessa Road–Bottaccione composite section (CR-BTT) has already been analyzed from magnetochron C24r up to the middle part of magnetochron C22r (Galeotti et al., 2010, 2017). In this work, we analyzed 16 samples aimed at detecting the exact stratigraphic positions of the C22r/C22n and C22n/C21r reversals at the BTT outcrop, in an interval between 63.6 and 78.4 m above the Cretaceous-Paleogene boundary, where they were expected to occur according to Lowrie et al. (1982). The rock-magnetic properties of the Scaglia Rossa Formation are well known (e.g., Lowrie et al., 1982), and paleomagnetic analyses were carried out following standard procedures (Kirschvink, 1980). The natural remanent magnetization (NRM), ranging from 3.665×10^{-4} A/m to 5.485×10^{-5} A/m, was thermally demagnetized in 15 steps up to a maximum temperature of 625 °C, where the samples appeared completely demagnetized. The remanent magnetization was measured after each heating step, using a 2G DC-SQUID cryogenic magnetometer hosted in a magnetically shielded room, and the characteristic magnetization was computed with principal component analysis using the PuffinPlot software package (Lurcock and Wilson, 2012). At least seven points were used to compute the characteristic magnetization.

From the S1 core, 143 paleomagnetic samples were collected at an ~30 cm average resolution. Samples were drilled perpendicularly to the vertical core axis, and therefore a dip of 0° was assigned to all cylindrical samples, as downhole logs indicate that the borehole did not deviate from the vertical by more than 2°–3°. Samples were then cut for NRM analysis (for more details, see Turtù et al., 2017).

All paleomagnetic measurements were conducted at the Alpine Laboratory of Paleomagnetism (ALP), Peveragno, Italy.

Geochemistry and Physical Properties

Bottaccione Section

$CaCO_3$ values (wt%) of 500 samples were analyzed at a 3 cm resolution from the interval spanning 63.6 m to 78.4 m above the Cretaceous-Paleogene boundary in the BTT section. Calcimetric analyses were carried out using a "Dietrich-Fruhling" calcimeter. The precision of measurements, based on replicate analyses, was within ±1%. Stable isotope analyses were carried out on bulk samples from the same interval at 6 cm resolution on a total of 250 samples. Carbon isotope analyses were performed at the Istituto per l'Ambiente Marino Costiero del Consiglio Nazionale delle Ricerche (IAMC-CNR) laboratory (Capo Granitola, Italy) using an automated continuous-flow carbonate preparation GasBench II device and a Thermo Electron Delta Plus V Advantage mass spectrometer. Analyses were conducted on powdered bulk rock samples after heating them to 400 °C to remove organic components. Replicate analyses provided a precision within ±0.06‰. Values were calibrated to the Vienna Peedee belemnite standard (VPDB) and converted to conventional delta notation ($\delta^{13}C$).

Smirra 1 Core

The magnetic susceptibility (MS) of the S1 core was measured using a Bartington magnetic susceptibility system mounted in the X-ray fluorescence (XRF) core scanner at the Royal Netherlands Institute for Sea Research (NIOZ). The MS2E high-resolution point-sensor has a footprint of 4 × 10 mm. Sensor drift correction algorithms were implemented in the Avaatech Magsus acquisition software (avaatech.com). Carbon stable isotope values were measured on 548 bulk sediment samples between 0 and 41 m depth. The cores were sampled at ~10 cm resolution using an 8 mm rock drill to collect dry powder sediment core samples in the limestone intervals. Samples from marly layers were collected by hand and were freeze-dried before crushing to obtain homogenized dry samples. Isotope measurements were carried out on 80–1000 µg of dry material at Utrecht University using a CARBO-KIEL automated carbonate preparation device linked to a Thermo-Finnigan MAT253 mass spectrometer and a Finnigan GasBench II, with an analytical precision of 0.04‰.

Spectral Analysis

Wavelet analysis was used to compute the evolutionary spectra of data series in the depth domain, using the wavelet script of Torrence and Compo (1998) and a Morlet mother wavelet with an order of 6. In the CR-BTT composite section, $CaCO_3$ content from the lower part of magnetochron C24r to the upper part of C21r was evaluated, and for the S1 core, the MS series was analyzed from the upper part of C22r to C21n. In addition, power spectral analysis of the BTT $CaCO_3$ record, after a second-order polynomial detrending, and of the MS record from the S1 core was conducted via the multitaper method (MTM) with three tapers and a time-bandwidth product of 2, using the Astrochron Package (Meyers, 2014); this approach allows for the identification of periodic components exceeding the 95% confidence level, according to the robust noise estimation algorithm of Mann and Lees (1996).

Seafloor Spreading Rates

The Umbria-Marche (U-M) age model obtained in this study, as well as other published age models such as that of Cande and Kent (1995), or CK95, the geologic time scale (GTS) 2004 (Ogg and Smith, 2004), GTS2012 (Ogg, 2012; Vandenberghe et al., 2012), and that of Westerhold et al. (2017), or Wetal17, were tested by constructing curves of the seafloor spreading rate using the database of magnetic anomaly width from Bouligand et al. (2006). To construct this database, sea-surface magnetic anomaly profiles were first corrected for the main magnetic field, reduced to the pole, and projected in the direction of seafloor spreading, and they were assumed to be constant in a given area (for details, see Bouligand et al., 2006). Geomagnetic reversals recorded by the oceanic crust were then located by searching for the maximum gradient along these profiles. The data used here came from the Indian, North Pacific, and South Pacific Oceans and originated from six main spreading centers (Fig. 2). For each spreading center, we estimated an averaged value and its 95% confidence interval for chron width (measured in the spreading rate direction) and then deduced from the age model the same quantities for the spreading rate. For spreading centers where data from both conjugate flanks were available, we first computed the averaged values and 95% confidence intervals of the half-spreading rates for each flank and then deduced the same quantities for the average of both flank values. This approach takes into account possible spreading asymmetry (e.g., Müller et al., 2008).

The method described here for estimating seafloor spreading curves is simpler than the usual method that relies on the estimation of the rotation parameters (e.g., Hellinger, 1981). We decided, however, to use the data set of Bouligand et al. (2006) because its temporal sampling

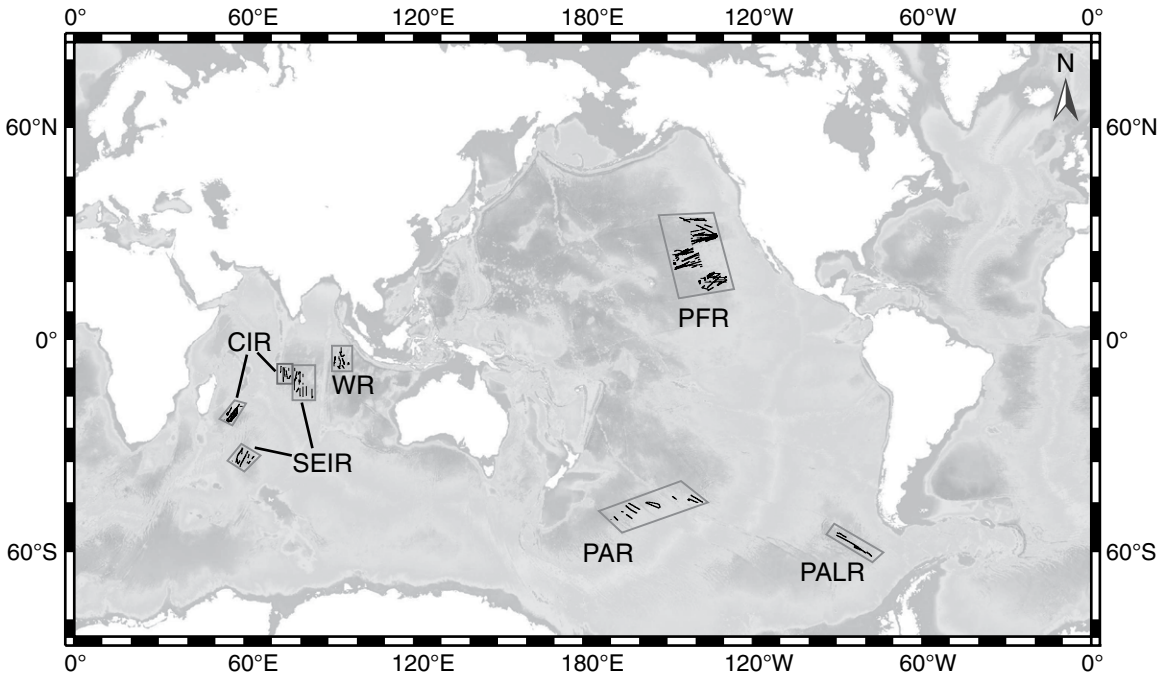

Figure 2. Location of selected areas (gray polygons) and magnetic profiles (black) over bathymetry from Smith and Sandwell (1997). Data originating from the same spreading center have been grouped together (see Royer and Sandwell, 1989; Cande and Patriat, 2015; Wright et al., 2016): CIR—Central Indian Ridge; SEIR—South East Indian Ridge; WR—Wharton Ridge; PFR—Pacific-Farallon Ridge; PAR—Pacific Antarctic Ridge; PALR—Pacific Aluk Ridge.

is larger than recently published seafloor spreading curves available for the Indian (Cande and Patriat, 2015) and Pacific Oceans (Wright et al., 2016b). Although the selected areas were characterized by a relatively constant spreading direction during the investigated period, some of the spreading rate variations deduced from the database of chron widths of Bouligand et al. (2006) could reflect small directional changes. For this reason, we also compared these curves with published spreading rates based on rotation parameters (Cande and Patriat, 2015; Wright et al., 2016b) that we adjusted to the different time scales.

The resolution of sea-surface magnetic profiles is limited by water depth, which is ~5000 m for the period 53.9–47.7 Ma investigated here (according to Parsons and Sclater, 1977). This resolution limit prevents us, using the method mentioned above, from correctly locating reversals that bound chrons with widths shorter than ~5000 m (i.e., ~125 k.y. for a seafloor spreading rate of 40 km/m.y.). This is due to the fact that sea-surface magnetic anomalies caused by such short chrons have a width controlled by the water depth (5000 m) and not by the true chron width. For this reason, for the construction of spreading rate curves, we did not include the reversals from very short subchrons C23n.1r and C24n.2n, the durations of which (51 k.y. and 100 k.y., respectively, in the new U-M age model) are shorter than the resolution of sea-surface magnetic profiles.

Comparison of Synthetic and Observed Magnetic Profiles

The durations of the short subchrons in C23n and C24n were tested by comparing the overall shape of stacks of observed magnetic anomaly profiles and synthetic profiles deduced from the age models with the assumption of a constant spreading rate and of a magnetized crust with a constant thickness and magnetization intensity. Before stacking, magnetic profiles were stretched between tie points (chron boundaries) to match the averaged chron width within each area. We used $C22r_{(base)}$, $C23n.1n_{(base)}$, $C23n.1r_{(base)}$, and $C23n.2n_{(base)}$ boundaries as tie points for chron C23n and $C23r_{(base)}$, $C24n.1n_{(base)}$, $C24n.2r_{(base)}$, and $C24n.3n_{(base)}$ boundaries for chron C24n. Synthetic profiles were computed at the pole (i.e., assuming a vertical direction for the magnetic field and magnetization), assuming that the seafloor topography followed the relation with age of Parsons and Sclater (1977), and using the algorithm of Talwani and Heirtzler (1964) with the method of Tisseau and Patriat (1981) to model off-axis intrusions and lava flows. We then shifted and rescaled the magnetic anomaly values in the stack to obtain a best fit (in the least-square sense) to the synthetic profiles, to assist with our comparison. This was needed because observed profiles were only partially corrected to the pole (correction of their skewness but not of their amplitude; for more details, see Bouligand et al., 2006) and possibly included the effect of a regional field that had not been corrected for, introducing a constant shift in the magnetic anomaly values. Finally, similarities between stacks and synthetic profiles were quantified by computing their Pearson correlation coefficients.

RESULTS

Bottaccione Section

Magnetostratigraphy

The results previously published by Galeotti et al. (2017) from the BTT section clearly show two reversals at 51.75–51.8 and 57.02–57.28 m above the Cretaceous-Paleogene boundary (Fig. 3A). As already identified by

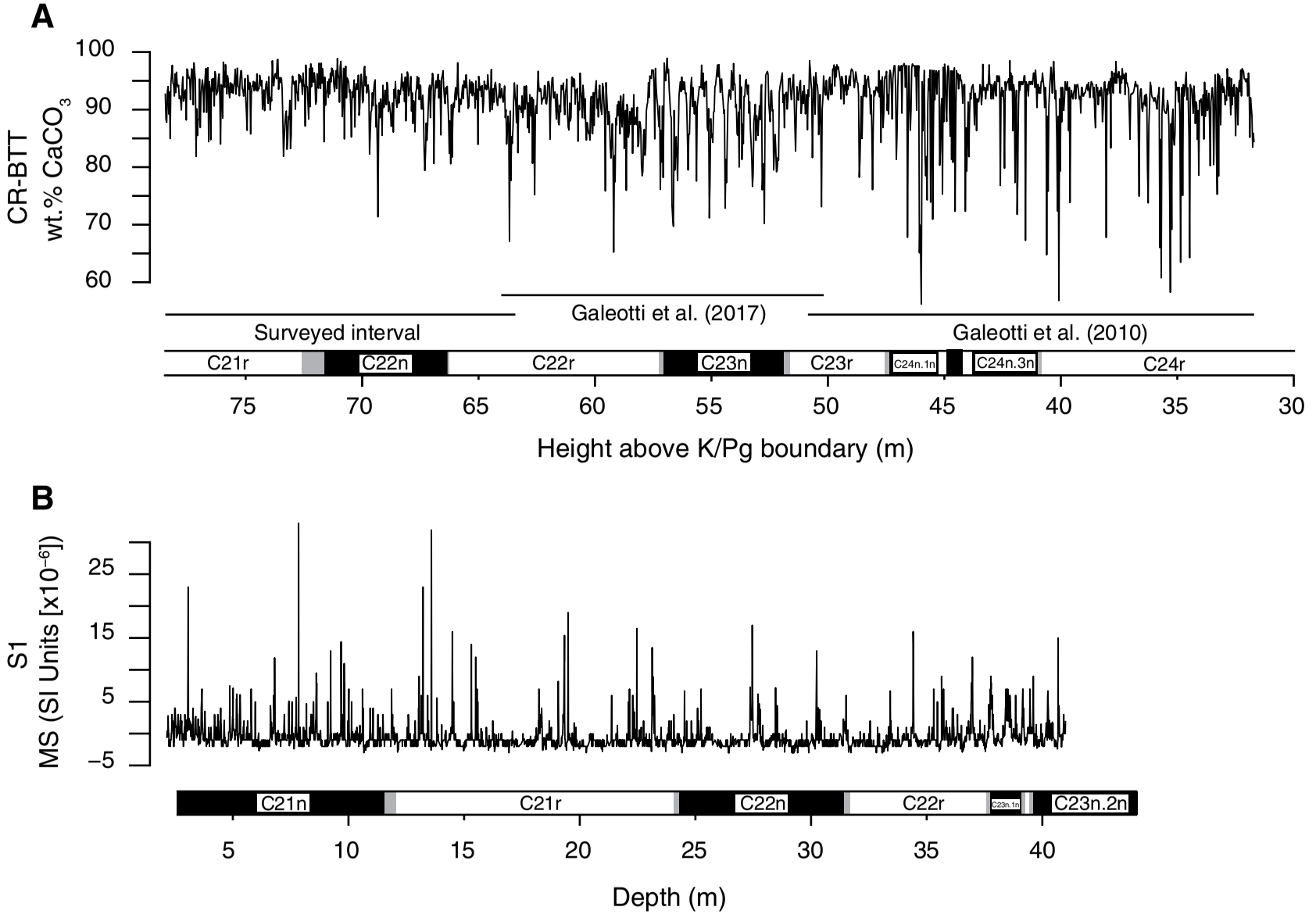

Figure 3. (A) $CaCO_3$ record (wt%) from the Contessa Road–Bottaccione (CR-BTT) composite section plotted against magnetostratigraphy. (B) Magnetic susceptibility (MS) values from Smirra 1 plotted against magnetostratigraphy. K/Pg boundary—Cretaceous-Paleogene boundary.

different authors (Arthur and Fischer, 1977; Napoleone et al., 1983), these two reversals correspond to the C23r/C23n and C23n/C22r magnetochron boundaries. In addition to the three magnetozones detected by Galeotti et al. (2017), we identified two additional reversals at 66.24–66.31 and 71.60–72.00 m above the Cretaceous-Paleogene boundary. In agreement with the original sampling of Arthur and Fischer (1977), the ~5.5-m-thick normal polarity interval between these magnetochron boundaries corresponds to magnetochron C22n. However, our paleomagnetic analysis does not allow us to define the top of this polarity chron with a precision better than ~40 cm, which corresponds to an ~50 k.y. uncertainty, considering the total duration of chron C22n (Cande and Kent, 1995).

Geochemistry

Geochemical records show a large variability across the surveyed interval, with $CaCO_3$ content ranging between ~68 and ~99 wt%, with an average value of ~92.8 wt% (Fig. 3A), and carbon isotope values ranging from ~1.0‰ to ~1.8‰, with CIEs up to ~0.5‰ (Fig. 4). On a long-term trend, following the rapid increase of average carbon isotope values in the upper half of C23n (Galeotti et al., 2017), $\delta^{13}C$ values vary across an average of ~1.5‰. Both records show an evident cyclicity, which has already been shown to be related to astronomical forcing both in the Umbria-Marche succession and oceanic records (Westerhold and Röhl, 2009; Galeotti et al., 2010, 2017; Westerhold et al., 2017). In particular, periods of depleted $\delta^{13}C$ values and concomitant impoverishment of $CaCO_3$ related to carbonate dissolution correspond to a maximal forcing (Lourens et al., 2005; Westerhold and Röhl, 2009; Galeotti et al., 2010, 2017; Westerhold et al., 2017).

Smirra 1 Core

Paleomagnetism

A detailed magnetic stratigraphy was obtained by identifying the characteristic remanent magnetization (ChRM). The newly produced paleomagnetic record of the S1 core, which spans from chron C21n to C23n (Turtù et al., 2017), is in good agreement with records obtained from other deep-sea cores for the same stratigraphic interval, allowing detailed comparison (Westerhold and Röhl, 2009; Galeotti et al., 2010, 2017; Sexton et al., 2011). In particular, the magnetostratigraphic record from S1 is consistent with BTT, and the thickness differences between magnetozones are generally limited to ~0.5 m. A larger discrepancy is observed for magnetochrons C22r and C22n, which are respectively ~2.5 m shorter and ~1.5 m longer compared to the same magnetochrons at the BTT section (Fig. 3B). These differences might be related to undetected tectonic deformation at Smirra, although no evidence of faulting can be observed in the cores nor in the optical logs (Turtù et al., 2017).

Bulk $\delta^{13}C$ and Magnetic Susceptibility Records

The bulk $\delta^{13}C$ record shows a large variability (Fig. 4). From the interval encompassing C23n.2n, average baseline carbon isotope values undergo a gradual increase of ~0.5‰, with heavier values persisting to the top of C21r, from which we can also observe a transition toward lighter values up to the top of the core. Superimposed on the long-term trends, the Smirra $\delta^{13}C$ record is punctuated by short-term negative CIEs, as found in coeval deep-sea records (Galeotti et al., 2010, 2017; Sexton et al., 2011; Kirtland Turner et al., 2014; Lauretano et al., 2016). These CIEs vary in amplitude between ~0.4‰ and ~1.0‰ and are associated with higher MS values.

GEOCHEMICAL CORRELATION OF THE UMBRIA-MARCHE RECORDS WITH OCEAN DRILLING PROGRAM SITES 1258 AND 1263

Carbon isotope records provide a robust means for intersite geochemical correlation, as hyperthermal events and dynamics regulating changes in seawater $\delta^{13}C$ have a global significance. We applied this exercise to the carbon isotope profiles of the S1 and BTT records for a local comparison, followed by their comparison with Ocean Drilling Program (ODP) Site 1258 at Demerara Rise (Sexton et al., 2011; Kirtland Turner et al., 2014) and ODP Site 1263 at Walvis Ridge (Lauretano et al., 2016; Fig. 4). We labeled prominent CIEs following Cramer et al. (2003) up to the lowermost magnetochron C23r, including H1 to L, and used the Lauretano et al. (2016) nomenclature between the middle C23r and the lower C22n chron, including M to W. For the rest of the studied interval (middle C22n to upper C21r), we followed the labeling of Sexton et al. (2011), revised by Westerhold et al. (2017). Comparison of the S1 with the BTT record shows a very good match of both the long-term trend and individual CIEs. Moreover, this carbon isotope stratigraphy correlation allows us to test the discrepancies observed in the thickness of the C22n and C22r magnetochrons between the two sites. In particular, a very good match of the $\delta^{13}C$ records is observed within C22n, which is ~1.5 m longer at Smirra. However, a slightly higher average sedimentation rate is observed at S1 (Turtù et al., 2017) compared to Bottaccione (Galeotti et al., 2010, 2017), and also for other magnetostratigraphic intervals. It is more difficult, thus, to explain the occurrence of a shorter C22r at Smirra. Furthermore, the carbon isotope record at BTT is characterized by two prominent CIEs, correlated with S and T of Lauretano et al. (2016), which are found at 59.2 m and 60.3 m above the Cretaceous-Paleogene boundary. Despite the easy recognition of these events at Bottaccione, we were not able to identify them at Smirra. Accordingly, the comparison between the carbon isotope records suggests that a gap of at least 3 m occurs in S1, even though there is no direct evidence for tectonic disturbance, but this does not exclude the possibility of a sedimentary hiatus or slump scar. By contrast, the U event (Lauretano et al., 2016), characterized by a prominent CIE that occurs in the upper part of magnetochron C22r, is well recognizable in both carbon isotope records. From there upward, the chemostratigraphic correlation between S1 and BTT is straightforward up to the middle part of chron C21r, as depicted in Figure 4. For this reason, the spectral analysis of S1 was performed only on the stratigraphic interval that spans 2.3–33 m. This still allowed us to build a composite and continuous cyclochronological record of CIEs from the Umbria-Marche Basin up to magnetochron C21n. Moreover, comparison of the Umbria-Marche record with ODP Site 1258 at Demerara Rise (Sexton et al., 2011; Kirtland Turner et al., 2014) and ODP Site 1263 at Walvis Ridge (Lauretano et al., 2016) shows a remarkably good match between the carbon isotope profiles, including both longer-term trends and CIEs within individual magnetochrons (Fig. 4). Minor differences are observed in the positions of a few CIE events with respect to the magnetostratigraphy at each site. Following the integration with the S1 record, we reexamined the stratigraphic position of each magnetochron in the CR-BTT composite record of Galeotti et al. (2017). This inspection revealed that all the magnetochrons have been correctly located in the spliced succession, with the exception of magnetochron C23n, which has been restudied and for which the upper limit occurs ~50 cm below the estimate of Galeotti et al. (2017), based on a splice with the record of Galeotti et al. (2010). Accordingly, C22rH1 or Q (Kirtland Turner et al., 2014; Lauretano et al., 2016) now consistently falls in the lowermost part of magnetochron C22r both at Smirra and Bottaccione, similar to what is observed at Sites 1258 and 1263 (Westerhold et al., 2017). However, C22nH1 or V (Kirtland Turner et al., 2014; Lauretano et al., 2016), which coincides with the C22r/C22n magnetochron boundary in the Umbria-Marche records, falls in the lowermost part of C22n at ODP Site 1263 (Lauretano et

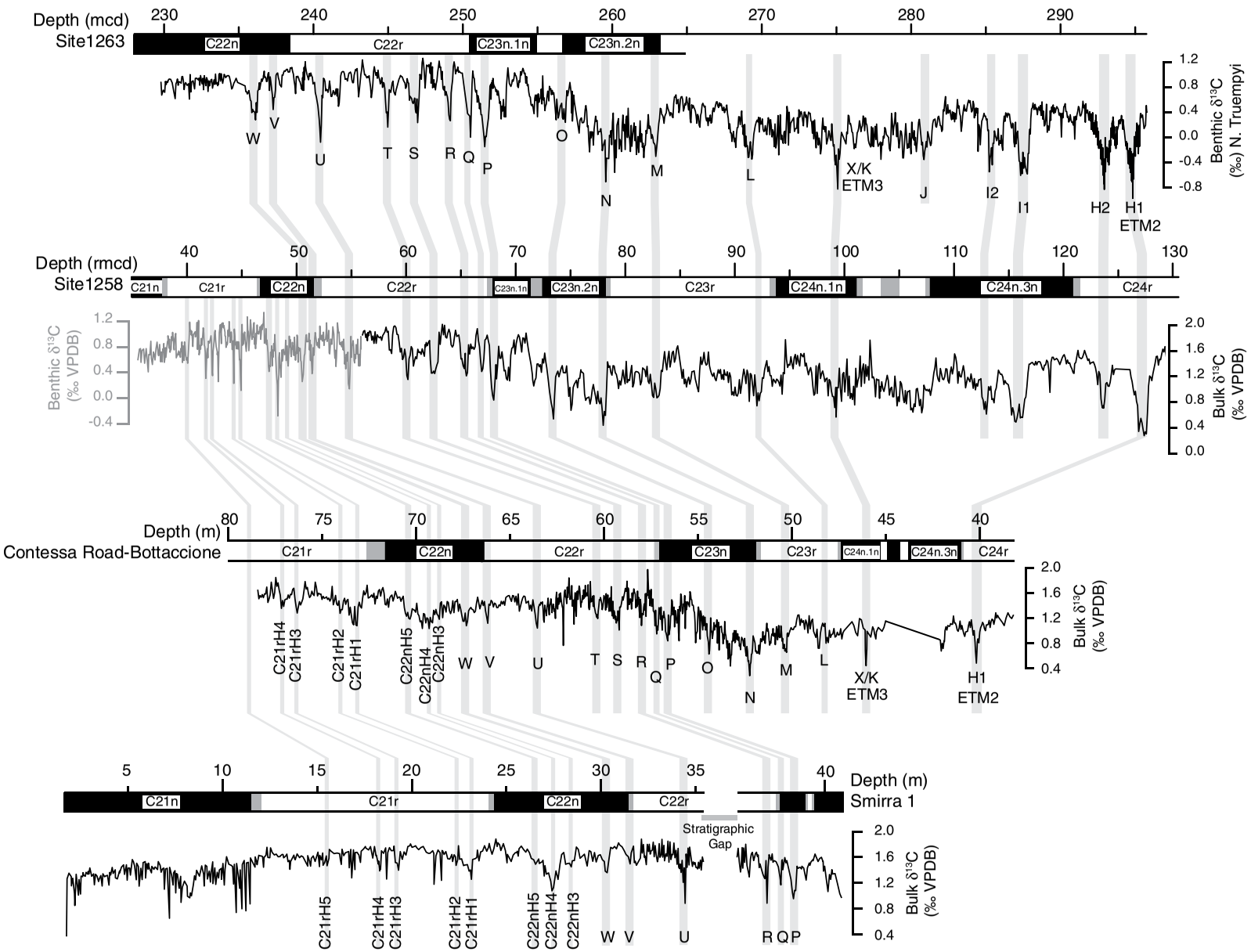

Figure 4. Chemostratigraphic ($\delta^{13}C$) and magnetostratigraphic correlations among Ocean Drilling Program (ODP) Site 1263 (Lauretano et al., 2016), ODP Site 1258 (Sexton et al., 2011 [gray line]; Kirtland Turner et al., 2014 [black line]), Contessa Road–Bottaccione composite section, and Smirra 1 core. Prominent carbon isotope excursions are labeled following Cramer et al. (2003) up to the lowermost magnetochron C23r, including H1 to L; Lauretano et al. (2016) nomenclature between the middle C23r and the lower C22n chron, including M to W; and Sexton et al. (2011), revised by Westerhold et al. (2017), for the rest of the section. ETM2—Eocene thermal maximum 2; ETM3—Eocene thermal maximum 3; VPDB—Vienna Peedee belemnite; N. truempyi—Nuttalides; mcd—meter composite depth; rmcd—revised meter composite depth.

al., 2016; Westerhold et al., 2017) and at ODP Site 1258 (Sexton et al., 2011; Kirtland Turner et al., 2014). Despite these minor differences in the position of the C22nH1/V event, the good alignment of the Umbria Marche record with those of ODP Site 1258 (Sexton et al., 2011; Kirtland Turner et al., 2014) and ODP Site 1263 (Lauretano et al., 2016; Westerhold et al., 2017) evidently results from the global significance of factors controlling the carbon cycle.

CYCLOSTRATIGRAPHY

Bottaccione Record

The wavelet spectrum of $CaCO_3$ content from the CR-BTT section reveals high spectral density above the 95% confidence limit corresponding to wavelengths of ~50 cm and ~2 m between 32 and 57 m (Fig. 5). These cycles have been linked to the short and long eccentricity cycles, respectively, by Galeotti et al. (2017). Much of the spectral power is centered at a longer wavelength of ~4.5 m, which, based on the analysis of the same succession, has been interpreted to track the long-term (~1.2 m.y.) modulation of obliquity (Galeotti et al., 2010; DeConto et al., 2012). This component is also evident in the amplitude modulation of the short eccentricity, which shows maxima at ~35, ~40, and 45 m, i.e., between ca. 55 and 52 Ma. A similar long-term modulation of the short eccentricity has been reported to occur in sedimentary cycles from various ODP sites across the same interval, possibly suggesting a transition from libration to circulation (Westerhold et al., 2017), which is contemplated in the La2010b and La2010c astronomical solutions (Laskar et al., 2011a). A large increase in sedimentation rate is clearly indicated in the wavelet spectrum at 57 m, observed as a shift in the wavelength of the dominant spatial cycles, corresponding to the C23n/C22r magnetochron boundary. From there upwards the interpreted astronomical components shift to lower frequencies, in line with an average sedimentation rate of ~0.85 cm/k.y. in the 8.5-m-thick C22r magnetochron, compared to ~0.5 cm/k.y. in the C23n magnetochron, based on the Cande and Kent (1995) geomagnetic polarity time scale. The wavelet spectrum shows a strong amplitude modulation of both the ~50 cm component up to ~57 m above the Cretaceous-Paleogene boundary and the ~90 cm component for the interval from 57 to 78.4 m above the Cretaceous-Paleogene boundary. Assuming that the ~50 cm cycles below 57 m and the ~90 cm cycles above represent short eccentricity, the observed amplitude modulation can be ascribed to the 405-k.y.-period eccentricity cycles being expressed by a wavelength of ~2 m up to the base of C23n and of ~3.5 m in the interval spanning the lowermost C22r to middle C21r magnetochron. Due to this, spectral analysis was conducted using only a little overlap with the interval analyzed by Galeotti et al. (2017), which was entirely characterized by an average sedimentation rate of ~0.5 cm/k.y.

MTM spectral analysis of the interval spanning 57–78.4 m above the Cretaceous-Paleogene boundary confirmed the interpretation of the wavelet analysis, with a spectral peak corresponding to a frequency of 0.265 cycles/m (wavelength of 380 cm) and a double peak at frequencies of ~0.85 and 1.15 cycles/m (wavelengths of 118 and 87 cm, respectively; Fig.

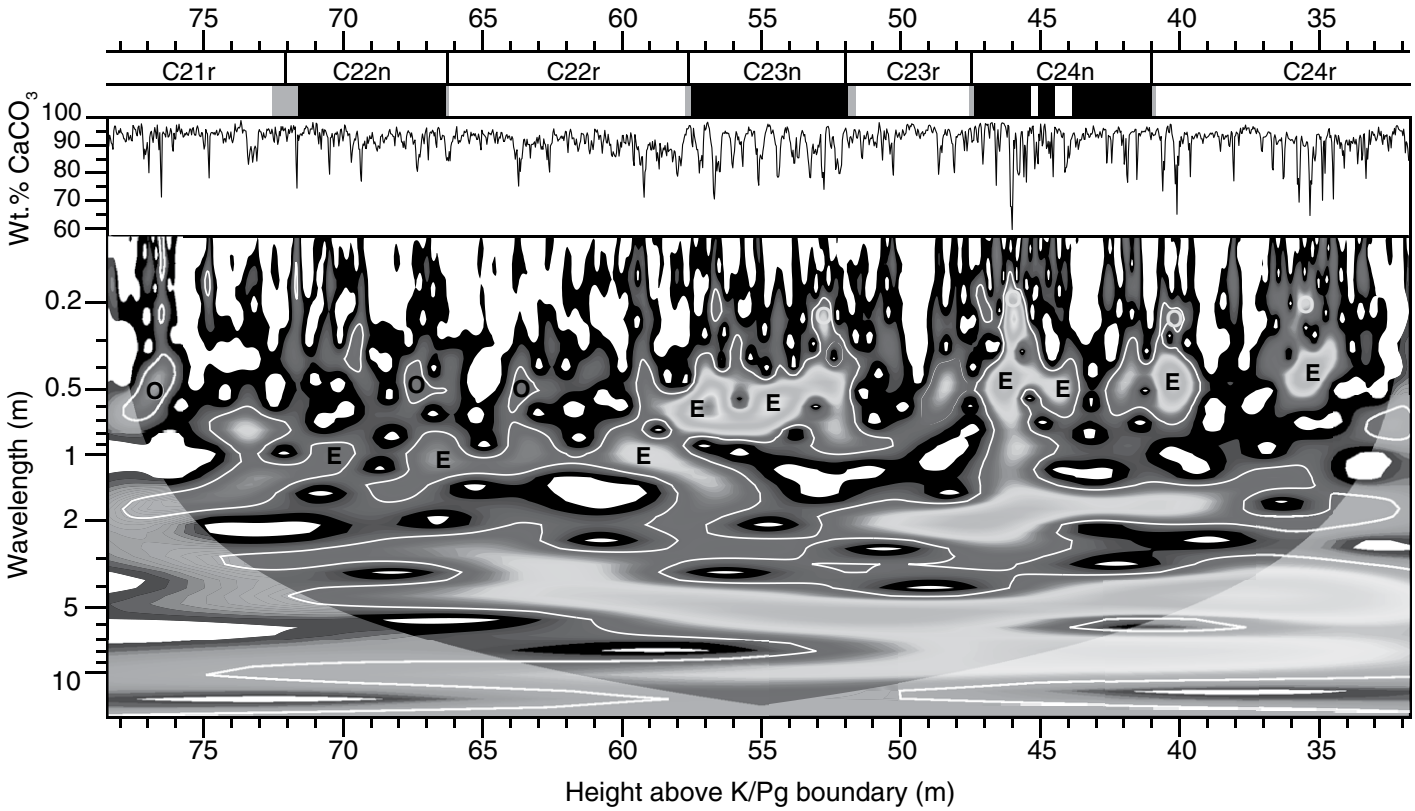

Figure 5. Evolutionary wavelet analysis for $CaCO_3$ content (wt%) from the Contessa Road–Bottaccione composite section for the interval spanning from 32 to 78.4 m above the Cretaceous-Paleogene boundary (K/Pg boundary) and magnetostratigraphy. White contours indicate the 95% confidence level for a red-noise model. "E" identifies the interpreted short eccentricity terms, and "O" identifies the interpreted obliquity terms.

6A). Based on an average sedimentation rate of ~0.85 cm/k.y., these frequencies are interpreted to represent the long eccentricity E1 term and the short eccentricity E2 and E3 terms, respectively. Astrochronological testing through the evolutive average spectral misfit technique (E-ASM; Meyers and Sageman, 2007; Meyers et al., 2012) on the Lower Eocene part of the CR-BTT composite section (Laurin et al., 2016) confirmed this interpretation.

On this basis, the spectral peaks occurring at frequencies of 2.15 and 2.62 cycle/m, corresponding to wavelengths of 46 cm and 38 cm, might represent the two main terms of obliquity (54 and 41 k.y.), although the 54 k.y. term is predicted to be weakly expressed in sedimentary records (Laskar et al., 2004). Spectral peaks are also present in the frequency range expected for precession, but these are not as clearly expressed as the peaks associated with eccentricity and obliquity.

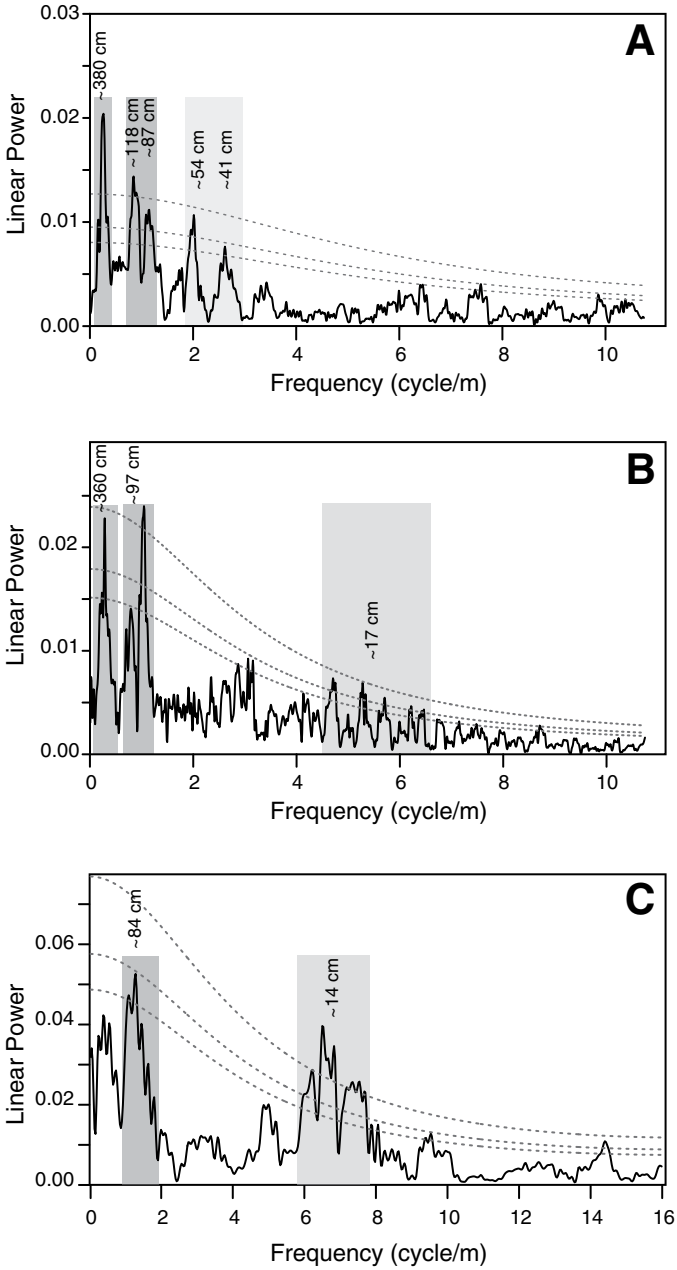

Figure 6. Results of multitaper method (MTM) spectral analyses carried out on the (A) $CaCO_3$ content from the Bottaccione section for the interval spanning 57–78.4 m above the Cretaceous-Paleogene boundary, (B) magnetic susceptibility (MS) values from Smirra 1 for the stratigraphic interval from 9 to 33 m, and (C) MS values from Smirra 1 for the stratigraphic interval from 2.3 to 9 m. Dashed lines represent the 90%, 95%, and 99% confidence levels for robust red noise (Mann and Lees, 1996).

Smirra 1 Core Record

The wavelet analysis of the MS record from the 2.3–33 m interval shows components, above the 95% confidence level, similar in frequency to the upper part at BTT. In particular, these components have wavelengths centered at ~100, ~40, and ~20 cm up to the lower part of C21n (Fig. 7). According to Cande and Kent (1995), the C22n–C21r magnetochron interval has an average sedimentation rate of 1.09 cm/k.y. On this basis, the observed components represent the sedimentary expression of the astronomical forcing related to short eccentricity, obliquity, and precession. A shift toward shorter wavelengths is observed at ~9 m up to the top of the record, within magnetochron C21n, suggesting a substantial decrease in sedimentation rate. Based on results from wavelet analysis, MTM analysis was carried out on two distinct stratigraphic segments spanning from 2.3 to 9 m and from 9 to 33 m (Fig. 6).

The MTM spectrum for the stratigraphic segment spanning from 9 to 33 m confirmed the interpretation of the wavelet analysis, providing evidence for distinct peaks exceeding the 95% confidence level with frequencies centered at ~0.278 and ~1.03 cycles/m, and five peaks centered at ~5.79 cycles/m (Fig. 6B). These frequencies correspond to cyclic components with wavelengths of 360, 97, and 17 cm, respectively. Based on the average sedimentation rate, this implies periods of ~400, ~100, and ~20 k.y., respectively. The best-fit sedimentation rate obtained using the TimeOpt routine (Meyers, 2015) on the MS record was ~1 cm/k.y., which provides further evidence that the periodic components revealed by MTM were astronomically controlled (Fig. 8).

MTM analysis of the upper segment (2.3–9 m) revealed distinct peaks exceeding the 90% confidence level at ~1.18 cycles/m (wavelength of 84 cm) and a dominant component exceeding the 99% confidence level centered at ~7.18 cycles/m (wavelength of 14 cm; Fig. 6C). The decrease in sedimentation rate detected by wavelet analysis suggests that these signals could be ascribed to the short eccentricity and precessional components, respectively. However, we did not include this interval in the final

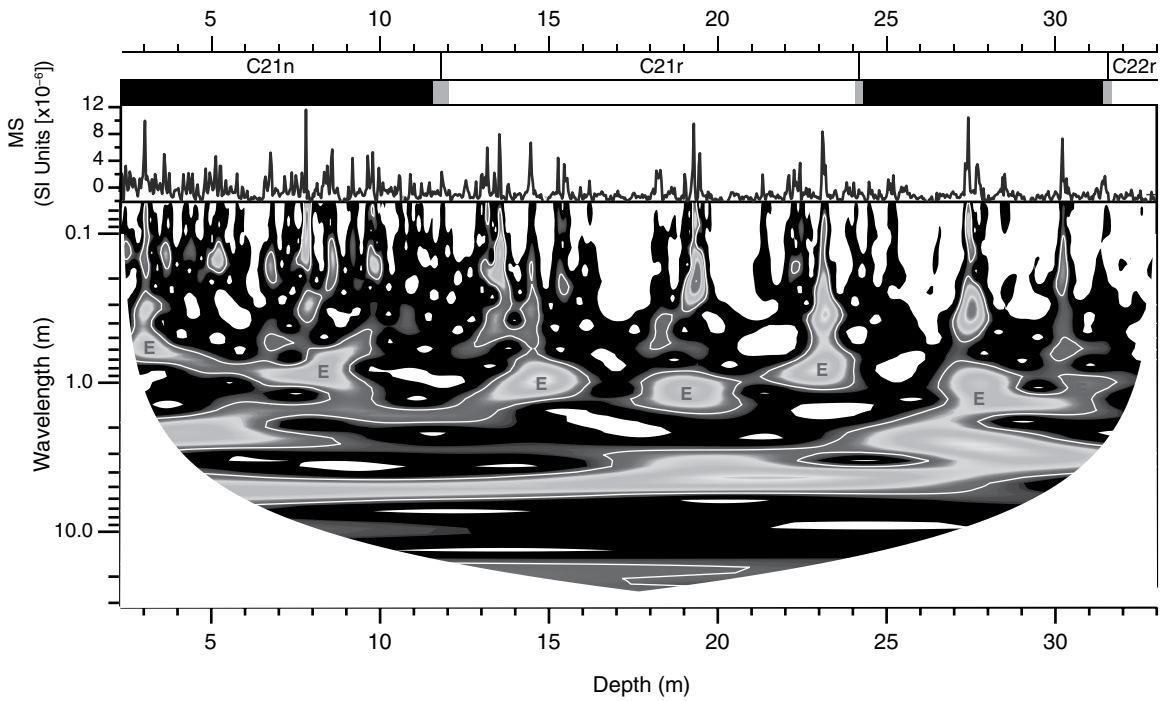

Figure 7. Evolutionary wavelet analysis for magnetic susceptibility (MS) values from the Smirra 1 for the interval spanning from 2.3 to 33 m. White contours indicate the 95% confidence level for a red-noise model. "E" identifies the interpreted short eccentricity terms.

astrochronology because of its limited thickness and because the available record does not reach the top of C21n.

ASTROCHRONOLOGY AND THE UMBRIA-MARCHE AGE MODEL

C22r–C21r Magnetochron Interval

To conduct the eccentricity-based cycle counting within the stratigraphic interval encompassing the C22r–C21r magnetochrons in the Umbria-Marche Basin, we used the cycle component corresponding to the long eccentricity (E1) term with a duration of 405 k.y. Based on the MTM spectral analysis results, a component with a wavelength of ~4 m was extracted from the $CaCO_3$ record of the BTT section and the MS record of S1 using the AnalySeries program (Paillard et al., 1996) and applying a Gaussian filter with a bandwidth of ±15%. This allowed us to establish a floating cyclochronology for the studied interval. Based on the obtained floating cyclochronology, we counted 2.75 and 1.75 405-k.y.-long cycles in magnetochrons C22r and C22n at BTT, respectively (Fig. 9). The same result was obtained for magnetochron C22n at S1, where we also counted 2.75 405-k.y.-long cycles in magnetochron C21r (Fig. 10). Filtering of the E2 and E3 short eccentricity components (~1 m wavelength) showed the expected amplitude modulation by the 405 k.y. eccentricity in both records. A very good match between the two sites was also obtained when comparing short eccentricity cycles across the overlapping interval, i.e., C22n, providing further evidence of the robustness of the cyclochronological interpretation. Assuming an average duration of 100 k.y. for the short eccentricity cycles, we obtained a total duration of 1010 k.y. and 700 k.y. for magnetochrons C22r and C22n, respectively. Because of uncertainty in the stratigraphic position of the top of C22n at BTT, the estimated duration of C22n is based only on the S1 record, where we counted seven complete short eccentricity cycles, for a total of 710 k.y. The S1 record allowed us to extend the cycle counting up to include magnetochron C21r, where we counted 12 short eccentricity cycles for a total of 1200 k.y.

The obtained cyclochronology provides the basis for an astronomical tuning of the Umbria-Marche record from the C22r to C21n magnetochrons. For this goal, we tuned the 405 k.y. eccentricity filtered component to the most recent astronomical solution of La2010b (Laskar et al., 2011a), allowing an optimal comparison with recently published results from the same time interval (Westerhold et al., 2017). Because of the absence of a clear long eccentricity cycle from the uppermost part of C23r to the uppermost part of C22r, we tuned the long eccentricity maxima identified from the amplitude and frequency modulations of the short eccentricity cycle, following the method reported by Laurin et al. (2016) and adopted by Galeotti et al. (2017). As a tie point, we used the age of the C23r/C23n magnetochron boundary, i.e., 51.78 Ma (Galeotti et al., 2017), corrected to 51.72 Ma, following a new linear age interpolation based on the observation of the maximal amplitude and frequency modulation interval of the E2 + E3 terms of eccentricity (Figs. 11 and 12).

Seafloor Spreading Rates

The U-M age model was tested by plotting seafloor spreading rate curves associated with different spreading centers in the Indian, North Pacific, and South Pacific Oceans (Fig. 13). Although the U-M age model encompasses only chrons C21n to C24n, spreading curves were computed for chrons C19r to C26n after merging our new age model with the ages from Wetal17 (from chrons C19r to C20r) and GTS2012 (from chrons C24r to C26n; see Table 1). For comparison, we also present similar spreading rate

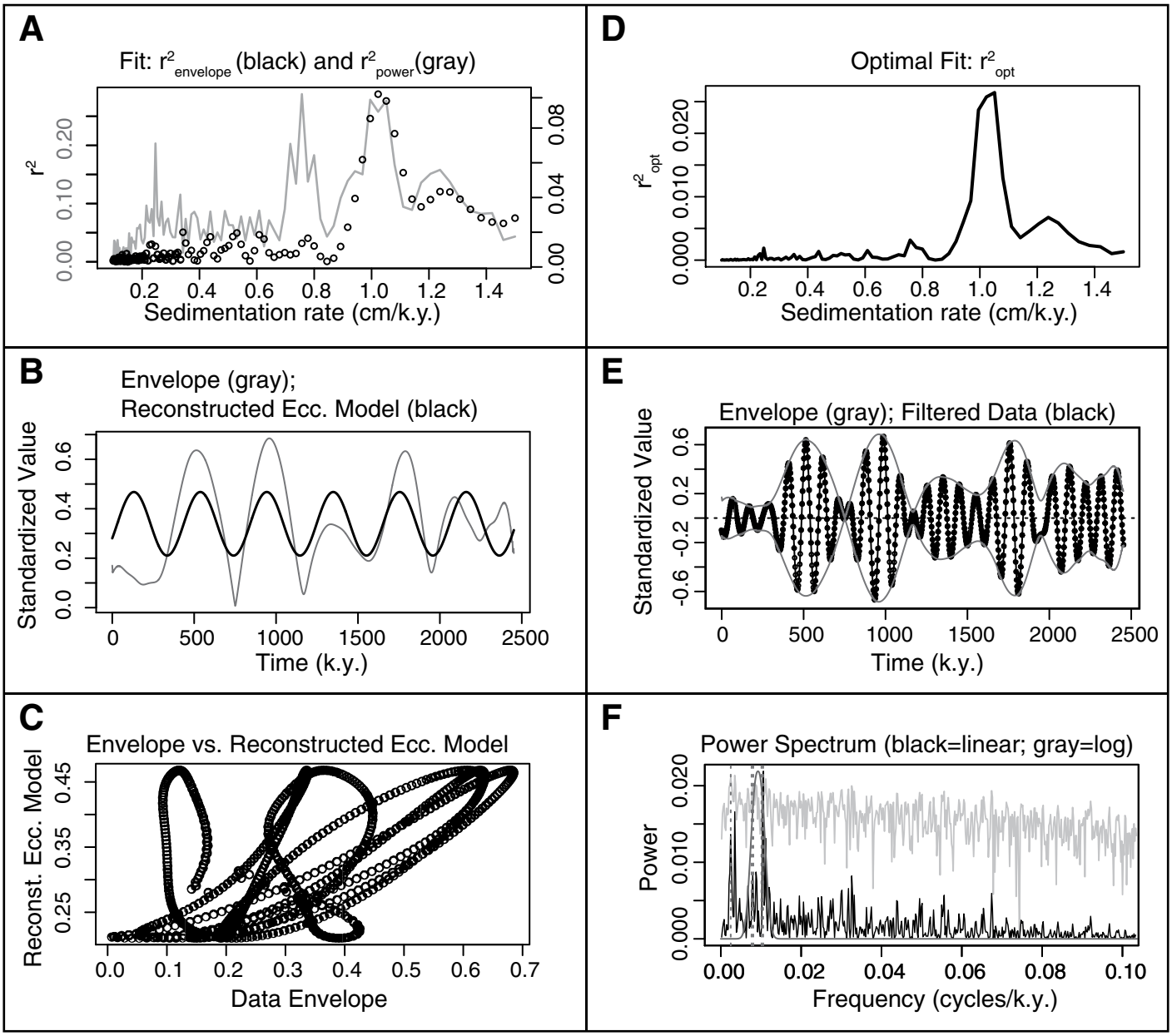

Figure 8. TimeOpt analysis on the magnetic susceptibility (MS) at Smirra 1 for the interval spanning from 9 to 33 m. (A) Squared Pearson correlation coefficient for the amplitude envelope fit (r^2 envelope, black dots) and the spectral power fit (r^2 spectral, gray line) at each evaluated sedimentation rate. (B) Comparison of the data amplitude envelope (gray) and the TimeOpt-reconstructed eccentricity model (black). (C) Cross plot of the data amplitude envelope and the TimeOpt-reconstructed eccentricity model in panel B. (D) Combined envelope and spectral power fit (r^2_{opt}) at each evaluated sedimentation rate. (E) Comparison of the band-passed eccentricity signal (black) and the data amplitude envelope (gray) determined via Hilbert transform. (F) Periodogram spectrum for the Bottaccione section, given the TimeOpt-derived sedimentation rate of ~1 cm/k.y. (black line—linear spectrum; gray line—log spectrum). Gray dashed lines indicate the eccentricity target periods.

curves using the CK95, GTS2004, GTS2012, and Wetal17 (merged with GTS2012 from chrons C24r to C26n) age models.

Figure 13 shows that spreading rates deduced from the chron width database of Bouligand et al. (2006) are generally consistent with spreading rate curves based on rotation parameters (Cande and Patriat, 2015; Wright et al., 2016b), where 95% confidence intervals generally overlap. Differences are nevertheless observed and may be due to the higher temporal sampling in the Bouligand et al. (2006) database, to small changes in spreading direction not taken into account in Bouligand et al. (2006), to the small number of profiles available for some chrons and areas in Bouligand et al. (2006; see Table 2), or to the distance between the flow lines used to predict the spreading rates from rotational parameters and the areas selected in Figure 2. For instance, data used for the Pacific Antarctic Ridge in Figure 2 are

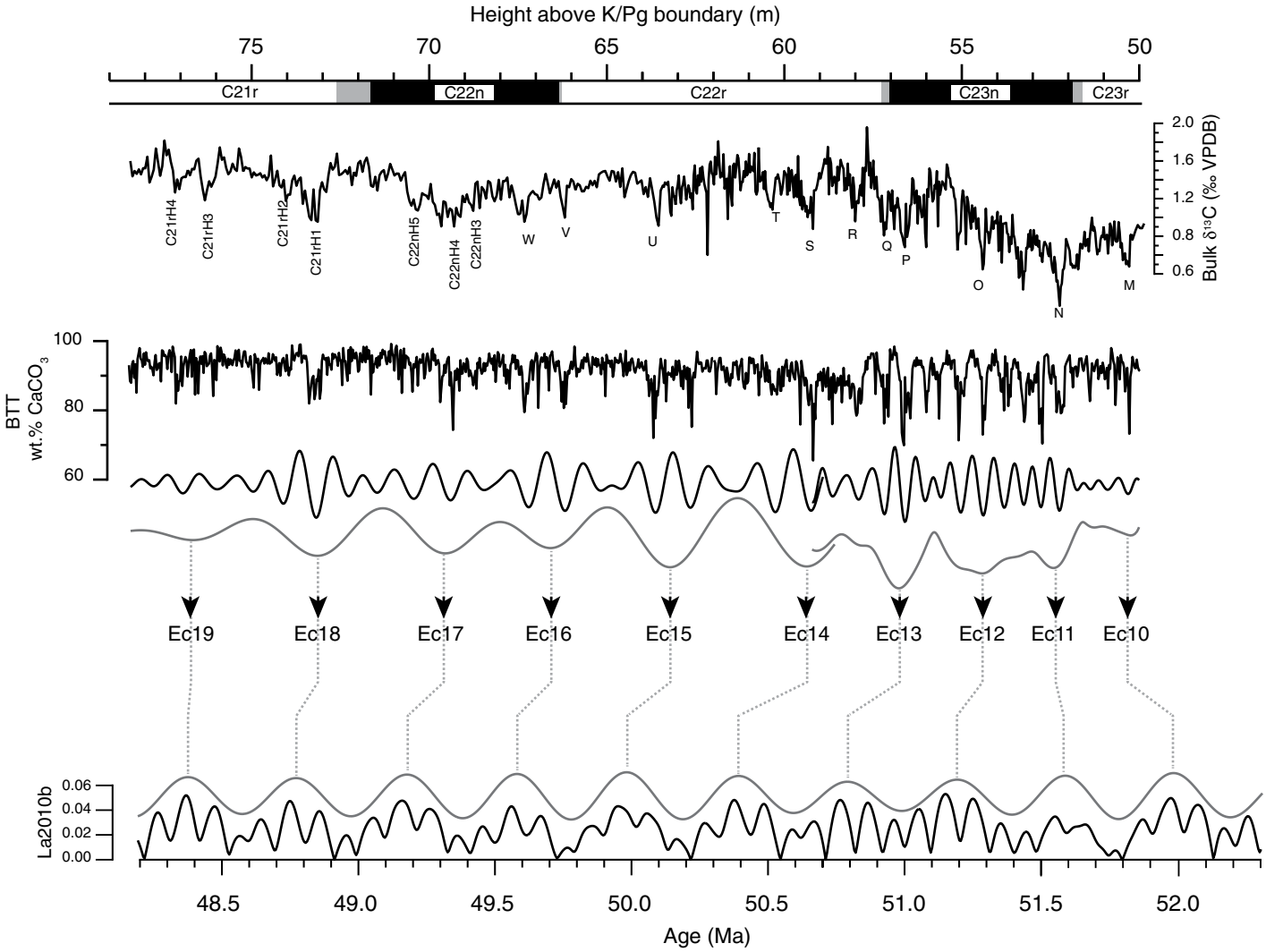

Figure 9. Long eccentricity (gray line) and short eccentricity (black line) filters for the interval spanning 50–78.4 m at Bottaccione (BTT) section plotted against the La2010b (Laskar et al., 2011a) astronomical solution. Long eccentricity maxima are labeled following the numbering of Galeotti et al. (2017). For the interval spanning the uppermost part of C23r to the uppermost part of C22r magnetochrons, we identified long eccentricity maxima and minima from the amplitude and frequency modulations of the short eccentricity term (Galeotti et al., 2017). VPDB—Vienna Peedee belemnite.

located north of the data and flow line used by Wright et al. (2016b). Note that spreading rate curves deduced from Cande and Patriat (2015) and Wright et al. (2016b) show only minor differences when computed for the recent U-M or Wetal17 age models, but they show significant differences when computed with previous age models (CK95, GTS2004, GTS2012). On the other hand, spreading curves obtained using the database of Bouligand et al. (2006) show significant differences for the U-M and Wetal17 age models, due to the higher temporal sampling. In the following, we will therefore only discuss the curves deduced from Bouligand et al. (2006).

Large temporal variations in seafloor spreading rates (by up to a factor of ~4) and in their uncertainty (represented by the 95% confidence intervals) are observed for all spreading centers (Fig. 13). The spreading rate uncertainty might be due to both uncertainties in reversal location and local variability in the seafloor spreading rate. Abrupt changes in spreading rates and larger than 95% confidence intervals are also often observed for short chrons, because their width and duration are characterized by larger relative uncertainties, and also because short-term variability in spreading rates may not have been averaged out due to the short duration of the chron. As noted earlier, our method for locating geomagnetic reversals is inadequate for reversals bounding chrons that are shorter than the spatial resolution of the sea-surface magnetic profiles (~5000 m). For such chrons, our method would tend to artificially increase the apparent chron width and spreading rate. We note, however, that the spreading rates in Figure 13 associated with short chrons, such as C25n or C26n, do not appear to be systematically higher, suggesting that these polarity events are not below the resolution of our sea-surface magnetic profiles.

Although the evolution of seafloor spreading rates shows significant differences among the different spreading centers (especially when

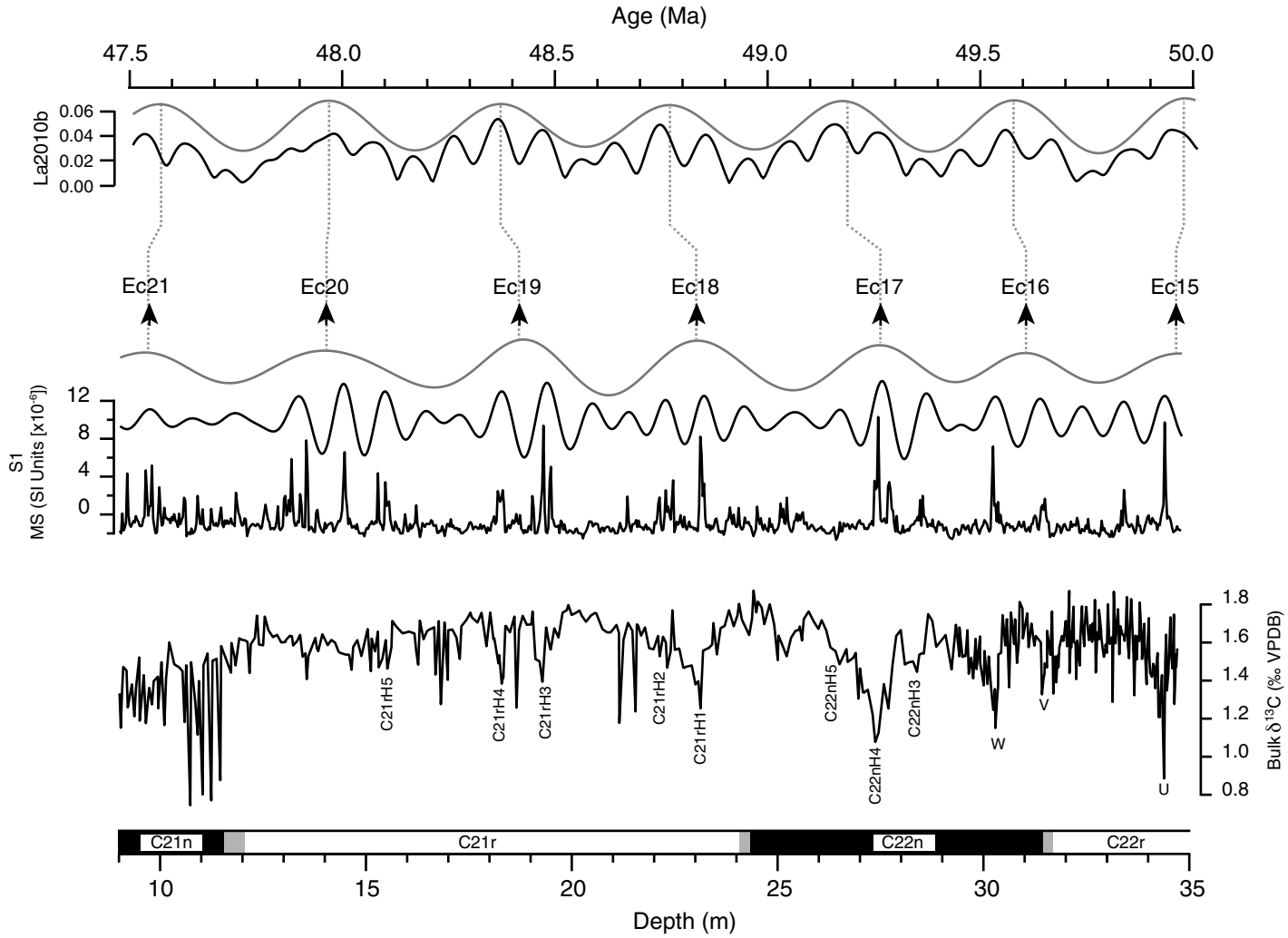

Figure 10. Long eccentricity (gray line) and short eccentricity (black line) filters for the interval spanning 35–9 m in the Smirra 1 core plotted against the La2010b (Laskar et al., 2011a) astronomical solution. Long eccentricity maxima are labeled following the numbering of Galeotti et al. (2017). VPDB—Vienna Peedee belemnite.

considering different oceans), we observe the existence of large deviations in spreading rates that are synchronous for all spreading centers, suggesting that these variations are not real, but instead reflect errors in the polarity time scale, which will be discussed further below. The spreading rate evolution deduced from the U-M age model shows significant differences from the evolution predicted by other polarity time scales. In particular, the new age model suggests the existence of periods of relatively constant spreading rates separated by rapid variations of spreading rate, while other age models suggest a rather gradual evolution of spreading rates (see, for instance, the C22n–C24n.1n interval for the Pacific Farallon Ridge and C22r–C24n.1n interval for the South East Indian Ridge).

DISCUSSION

We compared the U-M age model to other radioisotopic and astronomically calibrated age models. Cyclochronological interpretation of magnetochron C22r from the Umbria-Marche Basin is consistent with the estimate proposed by CK95, on the basis of anomaly profiles, which, in turn, agrees with the new estimate of Wetal17 from ODP Site 1258. This number is slightly different from that in GTS2004 and GTS2012, which both propose an ~300 k.y. longer duration for C22r. Cycle-counting across magnetochron C22n, the duration of which is 710 k.y. at S1 and 700 k.y. at BTT, is slightly shorter with respect to the estimate of GTS2004 (<100 k.y.). Moreover, in our cyclochronological interpretation, C21r is in line with the duration proposed in GTS2012, but it has an ~100 k.y. longer duration compared to CK95 and Wetal17, while it is slightly shorter with respect to GTS2004. The cyclochronological duration and the astrochronological ages of magnetochron boundaries and individual CIE events are reported in Tables 3, 4, and 5, along with previous estimates proposed by other authors. Compared to Galeotti et al. (2017), to which our time scale is tied via the astronomical age of the C23r/C23n magnetochron boundary (i.e., 51.78 Ma in Galeotti et al., 2017, slightly modified to 51.72 Ma), the age of some events around the C23n/C22r magnetochron boundary are different as the shape of the 405 k.y. filter changes based on the observation of a large sedimentation rate increase at the base of chron C22r. The largest differences with the most recent astrochronological estimates of

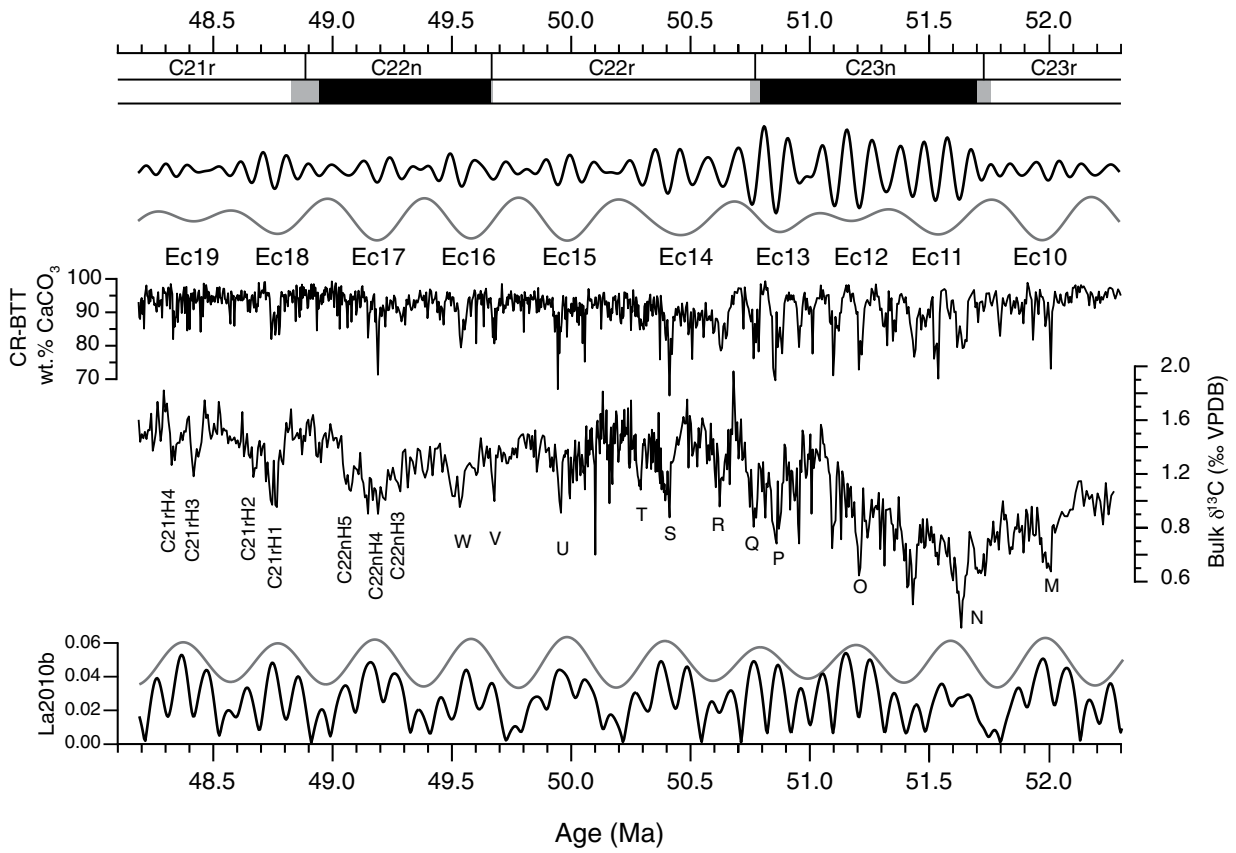

Figure 11. Astrochronologic calibration of the Contessa Road–Bottaccione (CR-BTT) composite section plotted against chemostratigraphic and magnetostratigraphic records. The tuning was performed using the ~4 m (E1) component. The lower panel represents the short eccentricity (black line) and long eccentricity (gray line) components extracted from the La2010b (Laskar et al., 2011a) astronomical solution. All components are reported in the time domain. Long eccentricity maxima are labeled following the numbering of Galeotti et al. (2017). VPDB—Vienna Peedee belemnite.

Wetal17 and Lauretano et al. (2016) are limited to one short eccentricity cycle across the C23n.2nH1, C22rH3, C21rH1, and C21rH2 events. Considering the good match between our astrochronology and that of Wetal17 at the resolution of the 405 k.y. cycles, the slightly different ages of these hyperthermal events can be ascribed to a slightly different interpretation of the relative position of individual geochemical events within each long eccentricity cycle. In the absence of a stable solution for short eccentricity in the studied time interval, this level of discrepancy is unavoidable. The astrochronological ages of the magnetochron boundaries show a very satisfactory match between our estimates and Wetal17, with moderate discrepancies at the C22n/C21r and C21r/C21n magnetochron boundaries that, in our astrochronological model, are 100 k.y. younger than reported by Westerhold et al. (2017).

In order to identify possible errors in the age models, we compared the spreading rate curves for different spreading centers as calibrated with different time scales (Fig. 13). In particular, large variations in spreading rates that are synchronous for all investigated spreading centers within the Indian and Pacific Oceans are unlikely and probably point to errors in the age models. As shown in Figure 13, chron C23r is systematically characterized by a higher spreading rate for CK95, GTS2004, and GTS2012, suggesting that the duration of this chron is too short in these age models. On the other hand, the Wetal17 and U-M age models suggest a shorter duration for chron C23r and do not show such a systematic increase in spreading rates associated with C23r. However, these two age models show rapid changes in spreading rate during chron C24n among all spreading centers, suggesting errors in the subchron durations. In particular, the ages of Wetal17 lead to very fast oscillations in spreading rate during this chron, whereas the U-M age model shows a systematic decrease in spreading rate for chron C24n.3n. However, it must be taken into account that these discrepancies in the U-M age model could be due to the sampling resolution, which is very close to the short duration of the subchrons.

The duration of subchrons within C24n and C23n was further investigated through a comparison of stacks of magnetic profiles and synthetic profiles deduced from the different age models (Fig. 14; Table 6). This comparison was only performed for the South East Indian Ridge, Central Indian Ridge, and Wharton Ridge in the Indian Ocean and for the Pacific Aluk Ridge in the South Pacific Ocean (see locations on Fig. 2), which are the only areas where the spreading rate was high enough to distinguish the anomalies associated with subchron C24n.2n. We first note that the synthetic profiles deduced from the previous polarity time scales, CK95, GTS2004, and GTS2012, already reproduced very well the stacks of profiles, especially in the Central Indian Ridge and South East Indian Ridge (Pearson correlation coefficient > 0.9). This is due

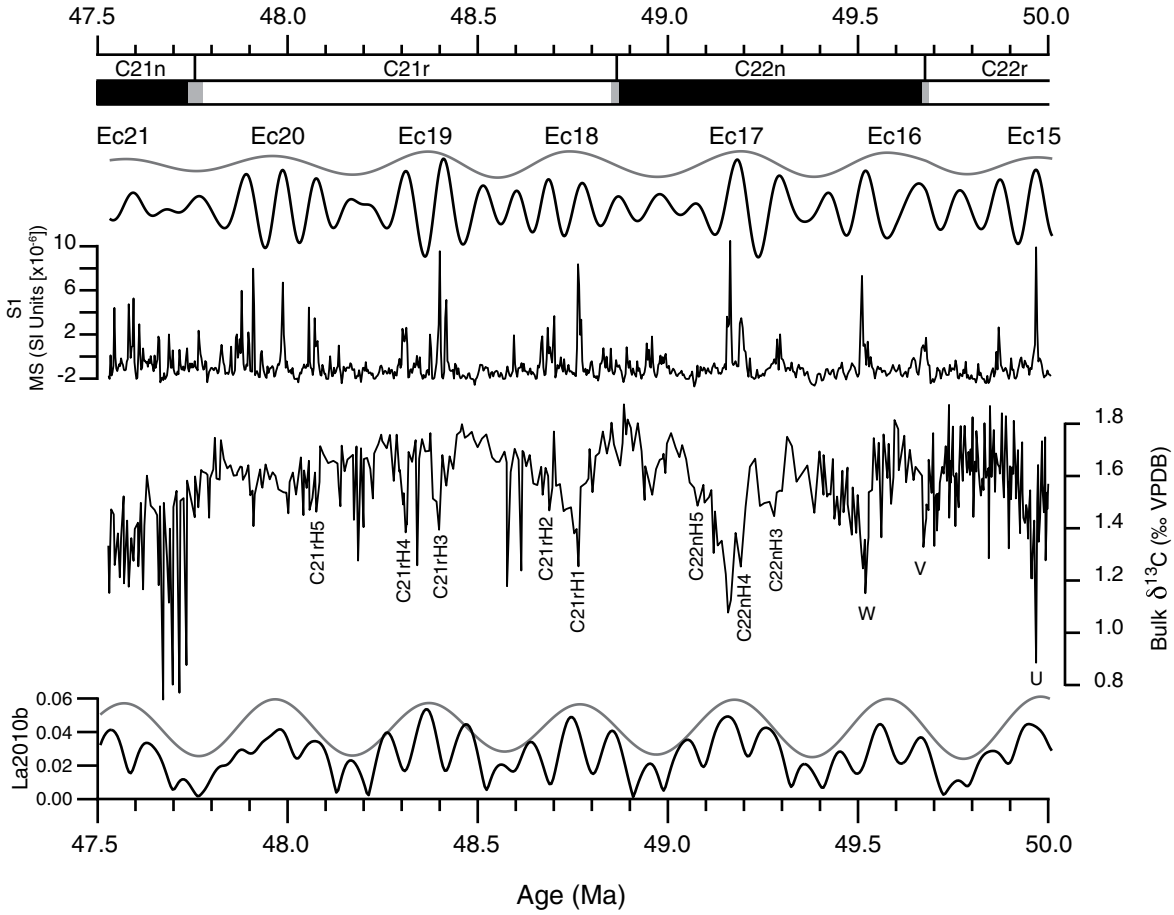

Figure 12. Astrochronologic calibration of the Smirra 1 core together with the bulk carbon isotope and magnetostratigraphic records. The tuning was performed using the ~360 cm (E1) component. The lower panel represents the short eccentricity (black line) and long eccentricity (gray line) from the La2010b (Laskar et al., 2011a) orbital solution. Long eccentricity maxima are labeled following the numbering of Galeotti et al. (2017). VPDB—Vienna Peedee belemnite; MS—magnetic susceptibility.

to the fact that the durations of short events in chrons C23n and C24n for these polarity time scales were derived using the sequence of magnetic anomaly widths compiled by Cande and Kent (1992), which for chrons C23n and C24n were based on a stack of two profiles from the Central Indian Ridge and South East Indian Ridge in the Indian Ocean. However, we notice some differences, the most obvious being the larger amplitude of anomaly C23n.1r in the synthetic profiles, suggesting that the duration of C23n.1r is too long in CK95, GTS2004, and GTS2012. Such discrepancies are due to the fact that only two magnetic profiles were used to constrain the durations of the C23n and C24n subchrons in these time scales, while we used stacks composed of a larger number of profiles (see number of profiles in Table 2). Looking now at the synthetic profiles deduced from the U-M age model, we see that this age model best reproduces the amplitude and location of the C23n.1r anomaly observed in the stacks (black dashed and solid curves) from the Indian Ocean compared to the other age models (largest Pearson correlation coefficient for C23n obtained with the U-M age model in Table 6). On the other hand, the synthetic profiles deduced from the U-M age model for chron C24n show significant differences with the observed stacks (with slightly lower Pearson correlation coefficients for C24n obtained with the U-M age model than with CK95, GTS2004, and GTS2012). In particular, we observe that the synthetic anomaly associated with C24n.2n has an amplitude about twice as large and is shifted toward younger ages compared to the stacks from the Indian Ocean. The difference in amplitude suggests that the duration of C24n.2n in the U-M age model (100 k.y.) is about twice too long, although this discrepancy could also be partly due to a lower intensity of Earth's magnetic field during the short polarity event C24n.2n. Note, however, that, because of the sampling resolution of ~30 cm for magnetostratigraphic samples, the uncertainty is ~25 k.y., which may explain some of the discrepancies. With respect to the temporal shift of C24n.2n, we notice that chron C24n corresponds to a period of increase in spreading rates at the South East Indian Ridge, Central Indian Ridge, and Wharton Ridge (Fig. 13). Since synthetic profiles in Figure 14 were computed assuming a constant spreading rate, the temporal shift of C24n.2n between the synthetic profiles and stacks might just reflect this increase in spreading rate. This is confirmed by the stack obtained for Pacific Aluk Ridge, in which the location of anomaly C24n.2n is more consistent with the U-M age model (Fig. 14; Table 6). A better estimation of the duration of subchrons within C24n would, however, re-

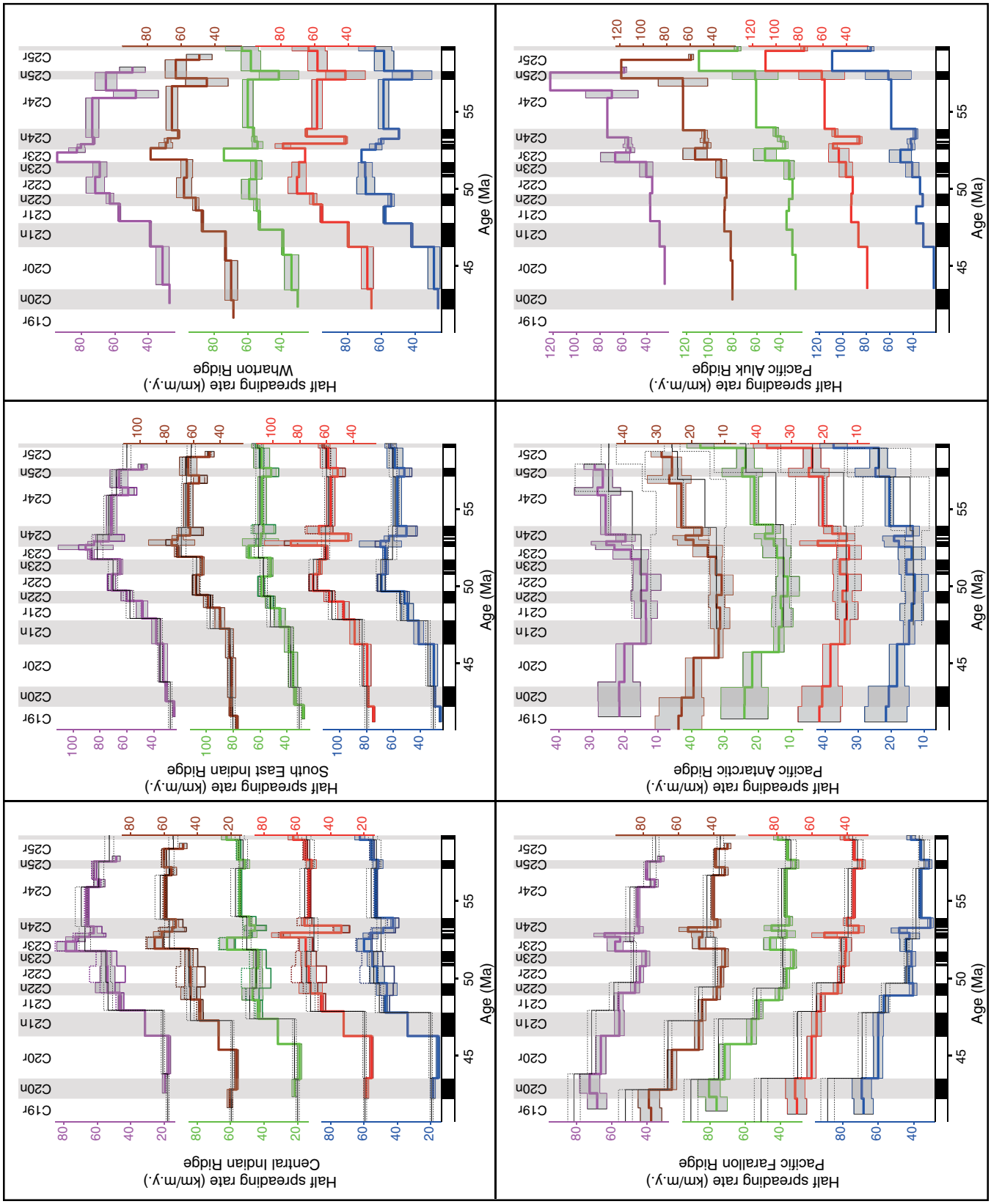

Figure 13.

TABLE 1. MAGNETOCHRON BOUNDARY AGES (MA)

Chron	CK95	GTS2004	GTS2012	Wetal17*	This study†
C19r $_{(base)}$	42.536	41.590	42.301	42.196	42.196
C20n $_{(base)}$	43.789	42.774	43.432	43.507	43.507
C20r $_{(base)}$	46.264	45.346	45.724	46.235	46.235
C21n $_{(base)}$	47.906	47.235	47.349	47.834	47.760
C21r $_{(base)}$	49.037	48.599	48.566	48.994	48.878
C22n $_{(base)}$	49.714	49.427	49.344	49.695	49.666
C22r $_{(base)}$	50.778	50.730	50.628	50.777	50.767
C23n.1n $_{(base)}$	50.946	50.932	50.835	50.942	50.996
C23n.1r $_{(base)}$	51.047	51.057	50.961	51.025	51.047
C23n.2n $_{(base)}$	51.743	51.901	51.833	51.737	51.724
C23r $_{(base)}$	52.364	52.648	52.620	52.628	52.540
C24n.1n $_{(base)}$	52.663	53.004	53.074	52.941	52.930
C24n.1r $_{(base)}$	52.757	53.116	53.199	53.087	53.020
C24n.2n $_{(base)}$	52.801	53.167	53.274	53.123	53.120
C24n.2r $_{(base)}$	52.903	53.286	53.416	53.403	53.250
C24n.3n $_{(base)}$	53.347	53.808	53.983	53.899	53.900
C24r $_{(base)}$	55.904	56.665	57.101	57.101	57.101
C25n $_{(base)}$	56.391	57.180	57.656	57.656	57.656
C25r $_{(base)}$	57.554	58.379	58.959	58.959	58.959
C26n $_{(base)}$	57.911	58.737	59.237	59.237	59.237

Note: CK95—Cande and Kent (1995); GTS2004—Geological Time Scale 2004 (Ogg and Smith, 2004); GTS2012—Geological Time Scale 2012 (Ogg, 2012; Vandenberghe et al., 2012); Wetal17—Westerhold et al. (2017); this study—Contessa Road–Bottaccione composite section and Smirra 1 core.
*Westerhold et al. (2017) merged with GTS2012 from chron C24r to chron C26n.
†CR-BTT and S1 merged with Westerhold et al. (2017) from chron C19r to chron C20r and GTS2012 from chron C24r to chron C26n.

TABLE 2. NUMBER OF PROFILES USED FOR DIFFERENT MAGNETOCHRONS

Chron	CIR*	SEIR*	WR	PFR	PAR	PALR
C19r	0	2 (2-0)	0	24	6	0
C20n	2 (0–2)	3 (3–0)	1	25	6	0
C20r	2 (0–2)	3 (3–0)	3	35	6	1
C21n	1 (0–1)	5 (5–0)	3	36	7	1
C21r	4 (2–2)	8 (7–1)	3	38	7	1
C22n	5 (2–3)	10 (7–3)	3	41	7	1
C22r	6 (2–4)	6 (4–2)	2	38	7	1
C23n	10 (3–7)	8 (5–3)	3	34	7	2
C23r	13 (5–8)	10 (5–5)	1	29	6	3
C24n.1n	12 (5–7)	9 (6–3)	3	28	5	3
C24n.1r–C24n.2r	12 (5–7)	9 (6–3)	3	28	5	3
C24n.3n	14 (5–9)	9 (6–3)	2	27	5	3
C24r	9 (4–5)	4 (2–2)	3	23	8	1
C25n	13 (3–10)	9 (4–5)	4	23	10	2
C25r	11 (3–8)	8 (4–4)	5	23	10	2
C26n	12 (4–8)	8 (4–4)	6	29	11	2

Note: CIR—Central Indian Ridge; SEIR—South East Indian Ridge, WR—Wharton Ridge; PFR—Pacific-Farallon Ridge; PAR—Pacific Antarctic Ridge; PALR—Pacific Aluk Ridge.
*Number of profiles for north and south flank are given in parentheses.

quire a detailed magnetostratigraphic study with a much higher sampling resolution, while the resulting durations could be tested with the use of high-resolution near-bottom marine magnetic profiles (as was done for chron C5, for instance, by Bowles et al., 2003).

The refinement of the polarity time scale and of the spreading rate curves during the early to middle Eocene is important for a better understanding of the cause of the seafloor spreading evolution during this period. Indeed, major absolute and relative plate motion changes are documented worldwide around 50 Ma (e.g., Müller et al., 2016). This includes, for instance, a significant decrease in spreading rates followed by a reorganization of spreading centers in the Indian Ocean near the onset of India-Eurasia collision (Patriat and Achache, 1984; Patriat and Segoufin, 1988; Cande and Patriat, 2015) and an increase of the Pacific-Farallon spreading rates following the complete subduction of the Izanagi plate (Whittaker et al., 2007; Seton et al., 2015) and the initiation of Izu-Bonin-Mariana subduction (Arculus et al., 2015). The bend in the Hawaii-Emperor chain occurred also near the same period, possibly reflecting both a change in the motion of the Hawaiian hotspot and in plate motion (Tarduno, 2007; Wright et al., 2015, 2016a; Wilson, 2016). Finally, ca. 50 Ma also coincides with the early Eocene climatic optimum, characterized by very high temperatures and pCO_2 values, followed by a long-term decrease in temperatures and pCO_2 during the Eocene (e.g., Zachos et al., 2001). Refinement of the polarity time scale is therefore critical to address important research questions such as the consequence of the worldwide plate motion reorganization for ocean chemistry, atmospheric pCO_2, and global climate on the long-term (10^6 yr) time scale (e.g., Kasting and Richardson, 1985; Rea et al., 1990; Müller et al., 2013, 2014; Norton and Lawver, 2014).

The U-M age model suggests a significantly different evolution of seafloor spreading rates than other age models (Fig. 13). In the Indian

Figure 13. Colored curves and gray bands represent averaged half-spreading rates and 95% confidence intervals, respectively, deduced from the magnetic profiles located in areas defined in Figure 2 and according to the age model of different authors (ordered from top to bottom): Cande and Kent (1995, purple line), Geologic Time Scale 2004 (GTS2004; Ogg and Smith, 2004, brown line), Geologic Time Scale 2012 (GTS2012; Ogg, 2012, green line), Westerhold et al. (2017, red line), and this study (Contessa Road–Bottaccione composite section and Smirra 1, blue line). Numbers of profiles used for each area and magnetochron are reported on Table 2. Note that 95% confidence intervals deduced from a small number of profiles may be artificially small and not representative of the overall spatial spreading rate variability and uncertainty. For Central Indian Ridge and South East Indian Ridge, the dark thick curves show the spreading rates associated with the north (solid line) and south (dotted lines) flanks. Black solid and dotted lines represent published spreading rate curves and their 95% confidence interval deduced from rotation parameters that have been adjusted to each age model (Central Indian Ridge and South East Indian Ridge from Cande and Patriat [2015] and Pacific-Farallon Ridge and Pacific Antarctic Ridge from Wright et al. [2016b]).

TABLE 3. MAGNETOCHRON BOUNDARY DURATIONS (K.Y.)

Chron	Standard GPTS			Cycle counting	Astronomically calibrated		Cycle counting*		Astronomically calibrated†	
	CK95	GTS 2004	GTS 2012	Lau3c§	Wetal17	Galetal17#	Bottaccione	Smirra 1	Bottaccione	Smirra 1
C21r	1131	1364	1217	N.D.**	1161	N.D.**	N.D.**	1200	N.D.**	1110
C22n	677	828	778	N.D.**	700	N.D.**	700	710	770	800
C22r	1064	1303	1284	N.D.**	1082	N.D.**	1010	N.D.**	1100	N.D.**
C23n	965	1171	1205	676	961	1180	1000	N.D.**	950	N.D.**
C23r	621	747	787	1016	890	760	840	N.D.**	820	N.D.**
C24n.1n	299	356	454	458	314	390	420#	N.D.**	390#	N.D.**
C24n.1r	94	112	125	162	145	90	N.D.**	N.D.**	90#	N.D.**
C24n.2n	44	51	75	67	36	100	N.D.**	N.D.**	1000#	N.D.**
C24n.2r	102	119	142	142	280	130	N.D.**	N.D.**	130#	N.D.**
C24n.3n	444	522	567	561	496	650	630#	N.D.**	650#	N.D.**
C24n $_{(total)}$	983	1160	1363	1390	1271	1360	1417#	N.D.**	1360#	N.D.**

Note: GPTS—geomagnetic polarity time scale; CK95—Cande and Kent (1995); GTS2004—Geological Time Scale 2004 (Ogg and Smith, 2004); GTS2012—Geological Time Scale 2012 (Ogg, 2012; Vandenberghe et al., 2012); Lau3c—three-cycle option of Lauretano et al. (2016); Wetal17—Westerhold et al. (2017); Galetal17—Galeotti et al. (2017).

*Floating time scale.

†Calibrated to Laskar 2010b astronomical solution (Laskar et al., 2011a).

§Three-cycle option taken from Lauretano et al. (2016).

#Galeotti et al. (2017).

**N.D.—not determined.

TABLE 4. MAGNETOCHRON BOUNDARY AGES (MA)

Chron	CR-BTT	S1	Wetal17
C21n $_{(base)}$	N.D.*	47.76	47.834
C21r $_{(base)}$	48.89	48.87	48.994
C22n $_{(base)}$	49.66	49.67	49.695
C22r $_{(base)}$	50.77	N.D.*	50.777
C23n $_{(base)}$	51.72	N.D.*	51.737
C23r $_{(base)}$	52.54	N.D.*	52.628
C24n.1n $_{(base)}$	52.93	N.D.*	52.941
C24n.1r $_{(base)}$	53.02	N.D.*	53.087
C24n.2n $_{(base)}$	53.12	N.D.*	53.123
C24n.2r $_{(base)}$	53.25	N.D.*	53.403
C24n.3n $_{(base)}$	53.90	N.D.*	53.899

Note: Age of magnetochron boundaries are listed according to this study (Contessa Road-Bottaccione section [CR-BTT] and Smirra 1 core [S1]) and most recent astrochronological estimates of Wetal17 (Westerhold et al., 2017).

*N.D.—not determined.

TABLE 5. HYPERTHERMAL EVENT AGES (MA)

Event	CR-BTT	S1	Lau3c*	Wetal17
PETM	56.10	N.D.†	N.D.†	55.93
ETM2	54.09	N.D.†	54.14	54.05
ETM3	52.80	N.D.†	52.83	52.84
L, C23rH1	52.44	N.D.†	52.41	52.46
M, C23rH2	52.00	N.D.†	51.88	51.97
N, C23n.2nH1	51.63	N.D.†	51.55	51.55
O, C23n.2nH2	51.21	N.D.†	51.28	51.23
P, C23n.1nH1	50.85	N.D.†	50.80	50.86
Q, C22rH1	50.76	N.D.†	50.73	50.76
R, C22rH2	50.62	N.D.†	50.63	50.67
S, C22rH3	50.40	N.D.†	50.47	50.48
T, C22rH4	50.29	N.D.†	50.32	50.37
U, C22rH5	49.96	49.96	49.96	49.95
V, C22nH1	49.67	49.67	49.70	49.68
W, C22nH2	49.53	49.52	49.6	49.58
C22nH3	49.29	49.29	N.D.†	49.38
C22nH4	49.19	49.19	N.D.†	49.25
C22nH5	49.08	49.07	N.D.†	49.14
C21rH1	48.76	48.77	N.D.†	48.85
C21rH2	48.66	48.69	N.D.†	48.76
C21rH3	48.41	48.40	N.D.†	48.45
C21rH4	48.32	48.31	N.D.†	48.36
C21rH5	N.D.†	48.08	N.D.†	48.07

Note: Age of hyperthermal events are listed according to this study (Contessa Road–Bottaccione section [CR-BTT] and Smirra 1 [S1] core) and the most recent astrochronological estimates of the three-cycle option of Lau3c (Lauretano et al., 2016) and Wetal17 (Westerhold et al., 2017). PETM—Paleocene-Eocene thermal maximum; ETM2—Eocene thermal maximum 2; ETM3—Eocene thermal maximum 3; L–W—carbon isotope excursions according to Cramer et al. (2003) and Lauretano et al. (2016).

*Three-cycle option taken from Lauretano et al. (2016).

†N.D.—not determined.

Figure 14. Comparison of stacks of marine magnetic profiles (black solid curves) from the Central Indian Ridge (CIR), South East Indian Ridge (SEIR), Wharton Ridge (WR), and Pacific Aluk Ridge (PALR) with synthetic anomaly profiles (gray solid curves) for chrons C23n and C24n. The synthetic profiles were obtained assuming a constant spreading rate (see value on the bottom-right corner of plots) and are predicted for different age models: Cande and Kent (1995, CK95), Geologic Time Scale 2004 (GTS2004; Ogg and Smith, 2004), Geologic Time Scale 2012 (GTS2012; Ogg, 2012), Westerhold et al. (2017, Wetal17), and this study (Umbria-Marche Basin [U-M]). The black dashed curve corresponds to the stacks after multiplying them by a constant factor and adding a constant vertical shift to obtain a best fit to the synthetic profiles in the least-square sense.

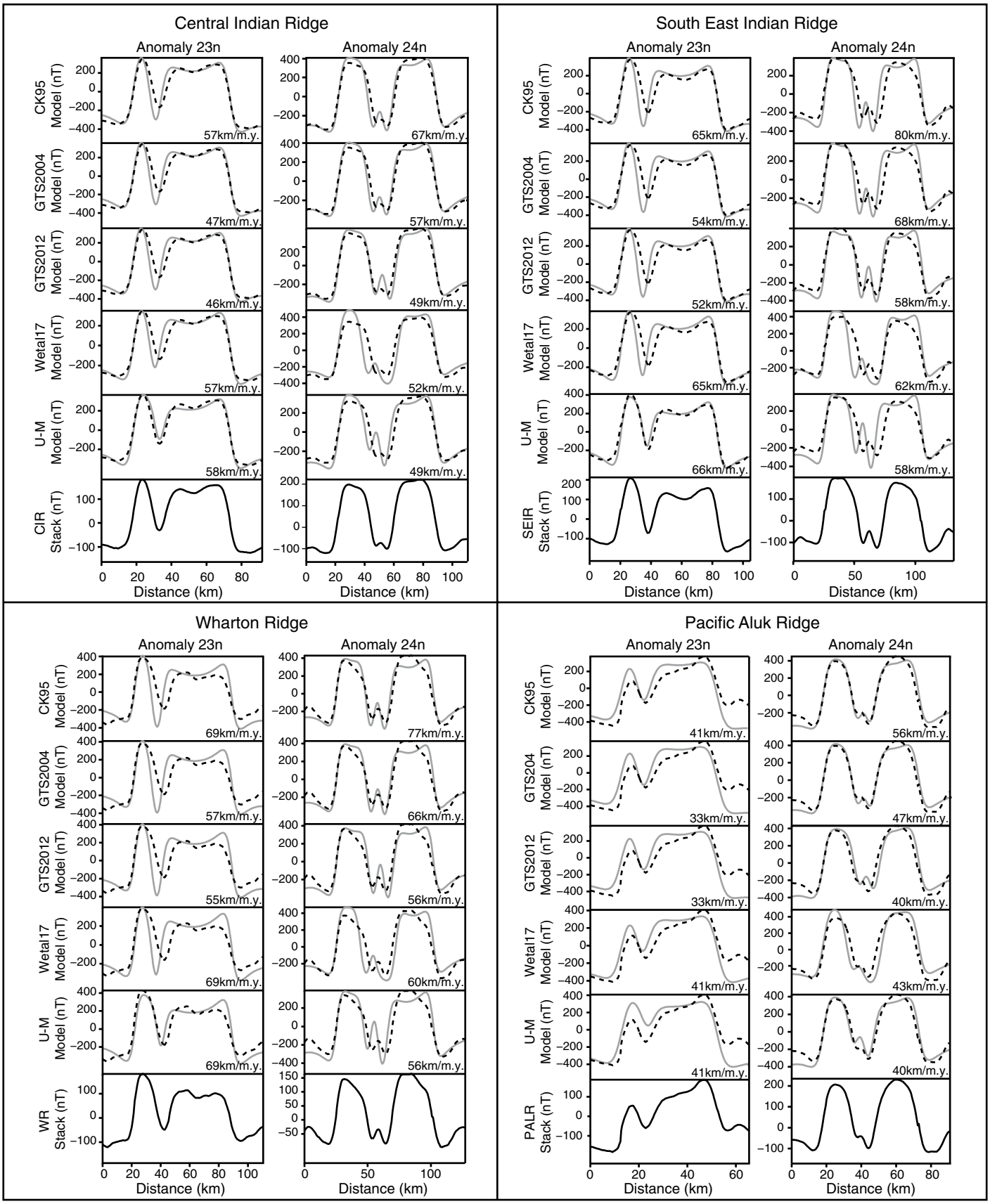

Figure 14.

TABLE 6. CORRELATION COEFFICIENTS

	C23n				C24n			
	WR	CIR	SEIR	PALR	WR	CIR	SEIR	PALR
CK95	0.86	0.97	0.93	0.85	0.96	0.98	0.91	0.98
GTS2004	0.86	0.97	0.93	0.85	0.96	0.98	0.92	0.98
GTS2012	0.86	0.97	0.93	0.85	0.95	0.98	0.96	0.96
Wetal17	0.85	0.96	0.92	0.87	0.92	0.92	0.90	0.94
U-M	0.94	0.99	0.99	0.85	0.92	0.95	0.85	0.97

Note: Pearson correlation coefficients between stacks and synthetic anomaly profiles are represented in Figure 14. WR—Wharton Ridge; CIR—Central Indian Ridge; SEIR—South East Indian Ridge; PALR—Pacific Aluk Ridge; CK95—Cande and Kent (1995) age model; GTS2004—Ogg and Smith (2004) geologic time scale; GTS2012—Ogg et al. (2012) geologic time scale; Wetal17—Westerhold et al. (2017) age model; U-M—Umbria-Marche Basin age model.

Ocean, the new age model suggests a period of constant spreading rate during chrons C23r to C22r, followed by a decrease in spreading rates after $C22n_{(base)}$ (ca. 50 Ma) for the South East Indian Ridge and Wharton Ridge. For the Central Indian Ridge, spreading rate seems to have slowly decreased from C23r to C21r, followed by a faster decrease after $C21n_{(base)}$ (ca. 48 Ma). In the North Pacific Ocean, the new age model suggests stepwise changes in spreading rates for the Pacific-Farallon Ridge, with the existence of several periods of constant spreading rates (chrons C24n.1n to C22n, chrons C21r to C20r, and possibly chrons C26n to C24r) separated by rapid changes in spreading rates (around $C21r_{[base]}$, i.e., ca. 49 Ma, and $C24n.2r_{[base]}$, i.e., ca. 53 Ma). These results tend to confirm that large oceanic plates are characterized by short periods of rapid changes separating long periods of constant or slowly changing spreading rates, as suggested by Wilson (1993) and Krijgsman et al. (1999) for the last 10 m.y. Defining the timing of changes in spreading rates (long-term vs. abrupt changes) is of particular interest because it might be an indicator of the different mechanisms involved (ridge-plume interactions vs. tectonic collision events).

CONCLUSIONS

The new integrated stratigraphic analysis from the Bottaccione section and Smirra core provides a continuous high-resolution record of the early to middle Eocene, spanning the Paleocene-Eocene thermal maximum to the lower part of magnetochron C21n. The carbon isotope analysis of the Umbria-Marche record allows the detection of carbon isotope excursions and their comparison with similar excursions observed in $\delta^{13}C$ records from other deep-sea settings, i.e., ODP Site 1258 and ODP Site 1263. The alignment of carbon isotope stratigraphies for the entire interval spanning C24r to C21n shows a very good match, reflecting the global dynamics of the carbon cycle, both on short and on long time scales. The lack of the C22rH3 and C22rH4 events at Smirra is interpreted to reflect a stratigraphic gap in magnetochron C22r.

Moreover, astronomically induced cyclicity has been detected in the $CaCO_3$ record of the Bottaccione section (from C22r to C21r magnetochron interval) and the MS record of the Smirra core (for the interval between magnetochrons C22r and C21r). The eccentricity-related cycles in the proxy records of the overlapping interval between the two Umbria-Marche sites reveal a very good match. These cycles were used to develop a floating cyclochronology and extend the existing astronomically calibrated age model for the Umbria-Marche Basin by 2.3 m.y. up to 47.5 Ma. This allows a comparison of the duration and the age of individual magnetochrons and events with other radioisotopic and astronomically calibrated age models. The astrochronological estimates across the C22r and C21r magnetochrons reveal durations that are in line with the estimates proposed by CK95 and Wetal17, but that are shorter with respect to GTS2004 and GTS2012. Magnetochron C22n, instead, is slightly shorter than in GTS2004, but it is in agreement with estimates in CK95, GTS2012, and Wetal17.

Spreading rates deduced from the Umbria-Marche model do not display large deviations that are correlated among the different ocean basins, with the exception of the subchrons in C24n, which will require a higher-resolution magnetostratigraphy to be resolved. We therefore conclude that the Umbria-Marche Basin records provide a valuable cyclochronological and astrochronological estimate for the duration of the interval spanning ca. 56 Ma to ca. 47 Ma.

The seafloor spreading rates deduced from the new age model suggest a significantly different evolution compared to other age models, and in particular point to the existence of rapid variations separating long periods of constant or slowly varying spreading rates. Refining the timing of these spreading rate changes is very important because it may help to determine the causative mechanism for such changes, especially around ca. 50 Ma, a period of worldwide changes in the seafloor spreading, which also coincides with the beginning of a long-term decrease in temperature and atmospheric pCO_2.

ACKNOWLEDGMENTS

This research benefited from funds provided by Ministero dell'istruzione, dell'Università e della Ricerca (MIUR)–Progetti di Ricerca di Interesse Nazionale (PRIN) grant 2010X3PP8J_005 to Galeotti and grant 2010X3PP8J_004 to Sprovieri, by a Ph.D. grant from the Italian Minister for Research to Francescone, by Netherlands Organisation for Scientific Research (NOW) Earth and Life Sciences (ALW) grant (project number 865.10.001) to Lourens, and by Netherlands Earth System Science Center (NESSC) grant 024.002.001 to Schrader and Lourens.

We thank Jérôme Dyment, who provided us with the code to compute synthetic profiles of marine magnetic anomalies. We are grateful to the Royal Netherlands Institute for Sea Research (NIOZ) and Rineke Gieles for technical help and analytical support. We thank Arnold van Dijk at Utrecht University for technical support. The database of magnetic anomaly picks from Bouligand et al. (2006) that we used in this study to construct spreading rate curves is deposited online at https://hal.archives-ouvertes.fr/hal-01812932. During the course of this study, C. Bouligand was a visiting scientist at the U.S. Geological Survey in Menlo Park, California, and benefited from a Congés pour Recherches ou Conversion Thématique (CRCT) from Conseil National des Universités (CNU; section 35) and a delegation to *Centre National de la Recherche Scientifique (France)*. The Institut des Sciences de la Terre (ISTerre) is part of Labex OSUG@2020 (ANR10 LABX56).

REFERENCES CITED

Arculus, R.J., Ishizuka, O., Bogus, K.A., Gurnis, M., Hickey-Vargas, R., Aljahdali, M.H., Bandini-Maeder, A.N., Barth, A.P., Brandl, P.A., Drab, L., et al., 2015, A record of spontaneous subduction initiation in the Izu-Bonin-Mariana arc: Nature Geoscience, v. 8, p. 728–733, https://doi.org/10.1038/ngeo2515.

Arthur, M.A., and Fischer, A.G., 1977, Upper Cretaceous–Paleocene magnetic stratigraphy at Gubbio, Italy: I. Lithostratigraphy and sedimentology: Geological Society of America Bulletin, v. 88, p. 367–371, https://doi.org/10.1130/0016-7606(1977)88<367:UCMSAG>2.0.CO;2.

Bouligand, C., Dyment, J., Gallet, Y., and Hulot, G., 2006, Geomagnetic field variations between chrons 33r and 19r (83–41 Ma) from sea-surface magnetic anomaly profiles: Earth and Planetary Science Letters, v. 250, p. 541–560, https://doi.org/10.1016/j.epsl.2006.06.051.

Bowles, J., Tauxe, L., Gee, J., McMillan, D., and Cande, S., 2003, Source of tiny wiggles in chron C5: A comparison of sedimentary relative intensity and marine magnetic anomalies: Geochemistry Geophysics Geosystems, v. 4, 1049, https://doi.org/10.1029/2002GC000489.

Cande, S.C., and Kent, D.V., 1992, A new geomagnetic polarity time scale for the Late Cretaceous and Cenozoic: Journal of Geophysical Research–Solid Earth, v. 97, no. B10, p. 13,917–13,951, https://doi.org/10.1029/92JB01202.

Cande, S.C., and Kent, D.V., 1995, Revised calibration of the geomagnetic polarity time scale for the Late Cretaceous and Cenozoic: Journal of Geophysical Research–Solid Earth, v. 100, p. 6093–6095, https://doi.org/10.1029/94JB03098.

Cande, S.C., and Patriat, P., 2015, The anticorrelated velocities of Africa and India in the Late Cretaceous and

early Cenozoic: Geophysical Journal International, v. 200, p. 227–243, https://doi.org/10.1093/gji/ggu392.

Cramer, B.S., Wright, J.D., Kent, D.V., and Aubry, M.P., 2003, Orbital climate forcing of $\delta^{13}C$ excursions in the late Paleocene–early Eocene (chrons C24n–C25n): Paleoceanography, v. 18, 1097, https://doi.org/10.1029/2003PA000909.

DeConto, R.M., Galeotti, S., Pagani, M., Tracy, D., Schaefer, K., Zhang, T., and Beerling, D.J., 2012, Past extreme warming events linked to massive carbon release from thawing permafrost: Nature, v. 484, p. 87–91, https://doi.org/10.1038/nature10929.

Dunkley-Jones, T., Lunt, D.J., Schmidt, D.N., Ridgwell, A., Sluijs, A., Valdes, P.J., and Maslin, M., 2013, Climate model and proxy data constraints on ocean warming across the Paleocene-Eocene thermal maximum: Earth-Science Reviews, v. 125, p. 123–145, https://doi.org/10.1016/j.earscirev.2013.07.004.

Galeotti, S., Angori, E., Coccioni, R., Ferrari, G., Galbrun, B., Monechi, S., Premoli Silva, I., Speijer, R., and Turi, B., 2000, Integrated stratigraphy across the Paleocene/Eocene boundary in the Contessa Road section, Gubbio (central Italy): Bulletin de la Société Géologique de France, v. 171, p. 355–365, https://doi.org/10.2113/171.3.355.

Galeotti, S., Krishnan, S., Pagani, M., Lanci, L., Gaudio, A., Zachos, J.C., Monechi, S., Morelli, G., and Lourens, L., 2010, Orbital chronology of early Eocene hyperthermals from the Contessa Road section, central Italy: Earth and Planetary Science Letters, v. 290, p. 192–200, https://doi.org/10.1016/j.epsl.2009.12.021.

Galeotti, S., Moretti, M., Cappelli, C., Phillips, J., Lanci, L., Littler, K., Monechi, S., Petrizzo, M.R., Premoli Silva, I., and Zachos, J.C., 2015, The Bottaccione section at Gubbio, central Italy: A classical Paleocene Tethyan setting revisited: Newsletters on Stratigraphy, v. 48, p. 325–339, https://doi.org/10.1127/nos/2015/0067.

Galeotti, S., Moretti, M., Sabatino, N., Sprovieri, M., Ceccatelli, M., Francescone, F., Lanci, L., Lauretano, V., and Monechi, S., 2017, Cyclochronology of the early Eocene carbon isotope record from a composite Contessa Road–Bottaccione section (Gubbio, central Italy): Newsletters on Stratigraphy, v. 50, p. 231–244, https://doi.org/10.1127/nos/2017/0347.

Hellinger, S.J., 1981, The uncertainties of finite rotations in plate tectonics: Journal of Geophysical Research–Solid Earth, v. 86, p. 9312–9318, https://doi.org/10.1029/JB086iB10p09312.

Huestis, S.P., and Acton, G.D., 1997, On the construction of geomagnetic time scales from non-prejudicial treatment of magnetic anomaly data from multiple ridges: Geophysical Journal International, v. 129, p. 176–182, https://doi.org/10.1111/j.1365-246X.1997.tb00947.x.

Kasting, J.F., and Richardson, S.M., 1985, Seafloor hydrothermal activity and spreading rates: The Eocene carbon dioxide greenhouse revisited: Geochimica et Cosmochimica Acta, v. 49, p. 2541–2544, https://doi.org/10.1016/0016-7037(85)90122-X.

Kennett, J.P., and Stott, L.D., 1991, Abrupt deep-sea warming, palaeoceanographic changes and benthic extinctions at the end of the Palaeocene: Nature, v. 353, p. 225–229, https://doi.org/10.1038/353225a0.

Kirschvink, J.L., 1980, The least-squares line and plane and the analysis of palaeomagnetic data: Geophysical Journal International, v. 62, no. 3, p. 699–718, https://doi.org/10.1111/j.1365-246X.1980.tb02601.x.

Kirtland Turner, S., Sexton, P.F., Charles, C.D., and Norris, R.D., 2014, Persistence of carbon release events through the peak of early Eocene global warmth: Nature Geoscience, v. 7, p. 748–751, https://doi.org/10.1038/ngeo2240.

Krijgsman, W., Hilgen, F.J., Raffi, I., Sierro, F.J., and Wilson, D.S., 1999, Chronology, causes and progression of the Messinian salinity crisis: Nature, v. 400, p. 652–655, https://doi.org/10.1038/23231.

Laskar, J., Robutel, P., Joutel, F., Gastineau, M., Correia, A.C.M., and Levrard, B., 2004, A long-term numerical solution for the insolation quantities of the Earth: Astronomy & Astrophysics, v. 428, p. 261–285, https://doi.org/10.1051/0004-6361:20041335.

Laskar, J., Fienga, A., Gastineau, M., and Manche, H., 2011a, La2010: A new orbital solution for the long-term motion of the Earth: Astronomy & Astrophysics, v. 532, p. A89, https://doi.org/10.1051/0004-6361/201116836.

Laskar, J., Gastineau, M., Delisle, J.B., Farrés, A., and Fienga, A., 2011b, Strong chaos induced by close encounters with Ceres and Vesta: Astronomy & Astrophysics, v. 532, p. L4, https://doi.org/10.1051/0004-6361/201117504.

Lauretano, V., Littler, K., Polling, M., Zachos, J.C., and Lourens, L.J., 2015, Frequency, magnitude and character of hyperthermal events at the onset of the early Eocene climatic optimum: Climate of the Past, v. 11, p. 1313–1324, https://doi.org/10.5194/cp-11-1313-2015.

Lauretano, V., Hilgen, F.J., Zachos, J.C., and Lourens, L.J., 2016, Astronomically tuned age model for the early Eocene carbon isotope events: A new high-resolution $\delta^{13}C$ benthic record of ODP Site 1263 between ~49 and ~54 Ma: Newsletters on Stratigraphy, v. 49, p. 383–400, https://doi.org/10.1127/nos/2016/0077.

Laurin, J., Meyers, S.R., Galeotti, S., and Lanci, L., 2016, Frequency modulation reveals the phasing of orbital eccentricity during Cretaceous oceanic anoxic event II and the Eocene hyperthermals: Earth and Planetary Science Letters, v. 442, p. 143–156, https://doi.org/10.1016/j.epsl.2016.02.047.

Lourens, L.J., Sluijs, A., Kroon, D., Zachos, J.C., Thomas, E., Röhl, U., Bowles, J., and Raffi, I., 2005, Astronomical pacing of late Palaeocene to early Eocene global warming events: Nature, v. 435, p. 1083–1087, https://doi.org/10.1038/nature03814.

Lowrie, W., Alvarez, W., Napoleone, G., Perch-Nielsen, K., Premoli Silva, I., and Toumarkine, M., 1982, Paleogene magnetic stratigraphy in Umbrian pelagic carbonate rocks: The Contessa sections, Gubbio: Geological Society of America Bulletin, v. 93, p. 414–432, https://doi.org/10.1130/0016-7606(1982)93<414:PMSIUP>2.0.CO;2.

Lurcock, P.C., and Wilson, G.S., 2012, PuffinPlot: A versatile, user-friendly program for paleomagnetic analysis: Geochemistry Geophysics Geosystems, v. 13, Q06Z45, https://doi.org/10.1029/2012GC004098.

Malinverno, A., Hildebrandt, J., Tominaga, M., and Channell, J.E.T., 2012, M-sequence geomagnetic polarity time scale (MHTC12) that steadies global spreading rates and incorporates astrochronology constraints: Journal of Geophysical Research–Solid Earth, v. 117, B06104, https://doi.org/10.1029/2012JB009260.

Mann, M.E., and Lees, J.M., 1996, Robust estimation of background noise and signal detection in climatic time series: Climatic Change, v. 33, p. 409–445, https://doi.org/10.1007/BF00142586.

McGowran, B., 1989, Silica burp in the Eocene ocean: Geology, v. 17, p. 857–860, https://doi.org/10.1130/0091-7613(1989)017<0857:SBITEO>2.3.CO;2.

Meyers, S.R., 2014, Astrochron: An R package for astrochronology: Available at cran.r-project.org/web/packages/astrochron/index.html.

Meyers, S.R., 2015, The evaluation of eccentricity-related amplitude modulation and bundling in paleoclimate data: An inverse approach for astrochronologic testing and time scale optimization: Paleoceanography, v. 30, no. 12, p. 1625–1640, https://doi.org/10.1002/2015PA002850.

Meyers, S.R., and Sageman, B.B., 2007, Quantification of deep-time orbital forcing by average spectral misfit: American Journal of Science, v. 307, p. 773–792, https://doi.org/10.2475/05.2007.01.

Meyers, S.R., Sageman, B.B., and Arthur, M.A., 2012, Obliquity forcing of organic matter accumulation during oceanic anoxic event 2: Paleoceanography, v. 27, no. 3, PA3212, https://doi.org/10.1029/2012PA002286.

Müller, R.D., Sdrolias, M., Gaina, C., and Roest, W.R., 2008, Age, spreading rates, and spreading asymmetry of the world's ocean crust: Geochemistry Geophysics Geosystems, v. 9, Q04006, https://doi.org/10.1029/2007GC001743.

Müller, R.D., Dutkiewicz, A., Seton, M., and Gaina, C., 2013, Seawater chemistry driven by supercontinent assembly, breakup, and dispersal: Geology, v. 41, p. 907–910, https://doi.org/10.1130/G34405.1.

Müller, R.D., Dutkiewicz, A., Seton, M., and Gaina, C., 2014, Seawater chemistry driven by supercontinent assembly, breakup and dispersal: REPLY: Geology, v. 42, p. e335, https://doi.org/10.1130/G35636Y.1.

Müller, R.D., Seton, M., Zahirovic, S., Williams, S.E., Matthews, K.J., Wright, N.M., Shephard, G.E., Maloney, K.T., Barnett-Moore, N., Hosseinpour, M., Bower, D.J., and Cannon, J., 2016, Ocean basin evolution and global-scale plate reorganization events since Pangea breakup: Annual Review of Earth and Planetary Sciences, v. 44, p. 107–138, https://doi.org/10.1146/annurev-earth-060115-012211.

Napoleone, G., Premoli Silva, I., Heller, F., Cheli, P., Corezzi, S., and Fischer, A.G., 1983, Eocene magnetic stratigraphy at Gubbio, Italy, and its implications for Paleogene geochronology: Geological Society of America Bulletin, v. 94, p. 181–191, https://doi.org/10.1130/0016-7606(1983)94<181:EMSAGI>2.0.CO;2.

Nicolo, M.J., Dickens, G.R., Hollis, C.J., and Zachos, J.C., 2007, Multiple early Eocene hyperthermals: Their sedimentary expression on the New Zealand continental margin and in the deep sea: Geology, v. 35, p. 699–702, https://doi.org/10.1130/G23648A.1.

Norton, I.O., and Lawver, L.A., 2014, Seawater chemistry driven by supercontinent assembly, breakup, and dispersal: COMMENT: Geology, v. 42, p. e334, https://doi.org/10.1130/G35109C.1.

Ogg, J.G., 2012, The geomagnetic polarity time scale, *in* Gradstein, F.M., Ogg, J.G., Schmitz, M.D., and Ogg, G.M., eds., The Geologic Time Scale 2012: Amsterdam, Netherlands, Elsevier, p. 85–113, https://doi.org/10.1016/B978-0-444-59425-9.00005-6.

Ogg, J.G., and Smith, A.G., 2004, The geomagnetic polarity time scale, *in* Gradstein, F.M., Ogg, J.G., and Smith, A.G., eds., A Geological Time Scale, 2004: Cambridge, UK, Cambridge University Press, 589 p.

Paillard, D., Labeyrie, L., and Yiou, P., 1996, Macintosh program performs time-series analysis: Eos (Washington, D.C.), v. 77, p. 379.

Pälike, H., and Hilgen, F., 2008, Rock clock synchronization: Nature Geoscience, v. 1, p. 282, https://doi.org/10.1038/ngeo197.

Parsons, B., and Sclater, J.G., 1977, An analysis of the variation of ocean floor bathymetry and heat flow with age: Journal of Geophysical Research, v. 82, p. 803–827, https://doi.org/10.1029/JB082i005p00803.

Patriat, P., and Achache, J., 1984, India-Eurasia collision chronology has implications for crustal shortening and driving mechanism of plates: Nature, v. 311, p. 615–621, https://doi.org/10.1038/311615a0.

Patriat, P., and Segoufin, J., 1988, Reconstruction of the Central Indian Ocean: Tectonophysics, v. 155, p. 211–234, https://doi.org/10.1016/0040-1951(88)90267-3.

Rea, D.K., Zachos, J.C., Owen, R.M., and Gingerich, P.D., 1990, Global change at the Paleocene-Eocene boundary: Climatic and evolutionary consequences of tectonic events: Palaeogeography, Palaeoclimatology, Palaeoecology, v. 79, p. 117–128, https://doi.org/10.1016/0031-0182(90)90108-J.

Röhl, U., Brinkhuis, H., Sluijs, A., and Fuller, M., 2004, On the search for the Paleocene/Eocene boundary in the Southern Ocean: Exploring ODP Leg 189 Holes 1171D and 1172D, Tasman Sea, *in* Exon, N.F., Kennett, J.P., and Malone, M.J., eds., The Cenozoic Southern Ocean: Tectonics, Sedimentation and Climate Change Between Australia and Antarctica: American Geophysical Union Geophysical Monograph 151, p. 113–125, https://doi.org/10.1029/151GM08.

Royer, J.Y., and Sandwell, D.T., 1989, Evolution of the eastern Indian Ocean since the Late Cretaceous: Constraints from Geosat altimetry: Journal of Geophysical Research: Solid Earth, v. 94, p. 13755–13782, https://doi.org/10.1029/JB094iB10p13755.

Seton, M., Flament, N., Whittaker, J., Müller, R.D., Gurnis, M., and Bower, D.J., 2015, Ridge subduction sparked reorganization of the Pacific plate–mantle system 60–50 million years ago: Geophysical Research Letters, v. 42, p. 1732–1740, https://doi.org/10.1002/2015GL063057.

Sexton, P.F., Norris, R.D., Wilson, P.A., Pälike, H., Westerhold, T., Röhl, U., Bolton, C.T., and Gibbs, S., 2011, Eocene global warming events driven by ventilation of oceanic dissolved organic carbon: Nature, v. 471, p. 349–352, https://doi.org/10.1038/nature09826.

Sluijs, A., Brinkhuis, H., Crouch, E.M., John, C.M., Handley, L., Munsterman, D., Bohaty, S.M., Zachos, J.C., Reichart, G.-J., Schouten, S., Pancost, R.D., Sinninghe Damsté, J.S., Welters, N.L.D., Lotter, A.F., and Dickens, G.R., 2008, Eustatic variations during the Paleocene–Eocene greenhouse world: Paleoceanography, v. 23, PA4216, https://doi.org/10.1029/2008PA001615.

Smith, W.H.F., and Sandwell, D.T., 1997, Global sea floor topography from satellite altimetry and ship depth soundings: Science, v. 277, p. 1956–1962, https://doi.org/10.1126/science.277.5334.1956.

Talwani, M., and Heirtzler, J.R., 1964, Computation of magnetic anomalies caused by two dimensional structures of arbitrary shape, *in* Parks, G., ed., Computers in the Mineral Industries: Stanford University Publications in Geological Sciences 9, p. 464–480.

Tarduno, J.A., 2007, On the motion of Hawaii and other mantle plumes: Chemical Geology, v. 241, p. 234–247, https://doi.org/10.1016/j.chemgeo.2007.01.021.

Tisseau, J., and Patriat, P., 1981, Identification des anomalies magnétiques sur les dorsales à faible taux d'expansion: Méthode des taux fictifs: Earth and Planetary Science Letters, v. 52, no. 2, p. 381–396, https://doi.org/10.1016/0012-821X(81)90191-6.

Torrence, C., and Compo, G.P., 1998, A practical guide to wavelet analysis: Bulletin of the American Meteorological Society, v. 79, p. 61–78, https://doi.org/10.1175/1520-0477(1998)079<0061:APGTWA>2.0.CO;2.

Tripati, A., and Elderfield, H., 2005, Deep-sea temperature and circulation changes at the Paleocene-Eocene thermal maximum: Science, v. 308, p. 1894–1898, https://doi.org/10.1126/science.1109202.

Turtù, A., Lauretano, V., Catanzariti, R., Hilgen, F.J., Galeotti, S., Lanci, L., Moretti, M., and Lourens, L.J., 2017, Integrated stratigraphy of the Smirra core (Umbria-Marche Basin, Apennines, Italy): A new early Paleogene reference section and implications for the geologic time scale: Palaeogeography, Palaeoclimatology, Palaeoecology, v. 487, p. 158–174, https://doi.org/10.1016/j.palaeo.2017.08.031.

Vandenberghe, N., Hilgen, F.J., Speijer, R.P., Ogg, J.G., Gradstein, F.M., Hammer, O., and Hooker, J.J., 2012, The Paleogene period, *in* Gradstein, F.M., Ogg, J.G., Schmitz, M.D., and Ogg, G.M., eds., The Geological Time Scale 2012: Amsterdam, Netherlands, Elsevier, p. 855–921.

Westerhold, T., and Röhl, U., 2009, High resolution cyclostratigraphy of the early Eocene—New insights into the origin of the Cenozoic cooling trend: Climate of the Past, v. 5, p. 309–327, https://doi.org/10.5194/cp-5-309-2009.

Westerhold, T., Röhl, U., Laskar, J., Raffi, I., Bowles, J., Lourens, L.J., and Zachos, J.C., 2007, On the duration of magnetochrons C24r and C25n and the timing of early Eocene global warming events: Implications from the Ocean Drilling Program Leg 208 Walvis Ridge depth transect: Paleoceanography, v. 22, PA2201, https://doi.org/10.1029/2006PA001322.

Westerhold, T., Röhl, U., and Laskar, J., 2012, Time scale controversy: Accurate orbital calibration of the early Paleogene: Geochemistry Geophysics Geosystems, v. 13, Q06015, https://doi.org/10.1029/2012GC004096.

Westerhold, T., Röhl, U., Frederichs, T., Agnini, C., Raffi, I., Zachos, J.C., and Wilkens, R.H., 2017, Astronomical calibration of the Ypresian time scale: Implications for seafloor spreading rates and the chaotic behavior of the solar system?: Climate of the Past, v. 13, p. 1129–1152, https://doi.org/10.5194/cp-13-1129-2017.

Whittaker, J.M., Muller, R.D., Leitchenkov, G., Stagg, H., Sdrolias, M., Gaina, C., and Goncharov, A., 2007, Major Australian-Antarctic plate reorganization at Hawaiian-Emperor bend time: Science, v. 318, p. 83–86, https://doi.org/10.1126/science.1143769.

Wilson, D.S., 1993, Confirmation of the astronomical calibration of the magnetic polarity time scale from sea-floor spreading rates: Nature, v. 364, p. 788–790, https://doi.org/10.1038/364788a0.

Wilson, D.S., 2016, Revision of Paleogene plate motions in the Pacific and implications for the Hawaiian-Emperor bend: COMMENT: Geology, v. 44, p. e384, https://doi.org/10.1130/G37388C.1.

Wright, N.M., Müller, R.D., Seton, M., and Williams, S.E., 2015, Revision of Paleogene plate motions in the Pacific and implications for the Hawaiian-Emperor bend: Geology, v. 43, p. 455–458, https://doi.org/10.1130/G36303.1.

Wright, N.M., Müller, R.D., Seton, M., and William, S.E., 2016a, Revision of Paleogene plate motions in the Pacific and implications for the Hawaiian-Emperor bend: REPLY: Geology, v. 44, p. e385, https://doi.org/10.1130/G37828Y.1.

Wright, N.M., Seton, M., Williams, S.E., and Müller, R.D., 2016b, The Late Cretaceous to recent tectonic history of the Pacific Ocean basin: Earth-Science Reviews, v. 154, p. 138–173, https://doi.org/10.1016/j.earscirev.2015.11.015.

Zachos, J.C., Pagani, M., Sloan, L., Thomas, E., and Billups, K., 2001, Trends, rhythms, and aberrations in global climate 65 Ma to present: Science, v. 292, p. 686–693, https://doi.org/10.1126/science.1059412.

Zachos, J.C., Röhl, U., Schellenberg, S.A., Sluijs, A., Hodell, D.A., Kelly, D.C., Thomas, E., Nicolo, M., Raffi, I., Lourens, J.L., McCarren, H., and Kroon, D., 2005, Rapid acidification of the ocean during the Paleocene-Eocene thermal maximum: Science, v. 308, p. 1611–1615, https://doi.org/10.1126/science.1109004.

Zachos, J.C., McCarren, H., Murphy, B., Röhl, U., and Westerhold, T., 2010, Tempo and scale of late Paleocene and early Eocene carbon isotope cycles: Implications for the origin of hyperthermals: Earth and Planetary Science Letters, v. 299, p. 242–249, https://doi.org/10.1016/j.epsl.2010.09.004.

Science Editor: Bradley S. Singer
Associate Editor: Stephen Meyers

Manuscript Received 11 March 2018
Revised Manuscript Received 2 August 2018
Manuscript Accepted 27 September 2018

Printed in the USA